Poeciliid Research

Quantitative multiscale analysis of spatial texture organization in liver histology of *Poecilia reticulata*

Ştefan Ţălu

The Directorate of Research, Development and Innovation Management (DMCDI),
The Technical University of Cluj-Napoca, Cluj-Napoca, Romania.
Corresponding author: Ş. Ţălu, stefan.talu@auto.utcluj.ro

https://doi.org/10.67784/0101

Abstract. Quantitative characterization of liver histology requires analytical approaches capable of describing spatial heterogeneity and directional organization beyond conventional visual assessment and global intensity statistics. This study presents an exploratory multiscale texture analysis of four published liver histology panels of *Poecilia reticulata* reported in a study investigating co-exposure to iron oxide nanoparticles and glyphosate-based herbicides. The original investigation documented hepatic histopathological alterations using complementary histological, histochemical, and ultrastructural methods. Building on this biological context, the present study examines image-derived texture properties without assuming that individual descriptors directly measure specific lesions or toxicological mechanisms. Ten complementary texture descriptors were evaluated at four Gaussian scales and four orientations and organized into a multidimensional descriptor tensor (160 entries per panel for a single global region of interest, and 640 entries per panel for a four-region partition). Global measurements and regional analysis were used to investigate scale-dependent responses, directional anisotropy, spatial heterogeneity, and inter-descriptor relationships. In the analysed panels, the control panel (A) and the vasocongested panel (B) showed measurable directional organization (sampled anisotropy index A_4 = 0.19 and 0.18 at s = 2 px), with texture axes near 93° and 177°, whereas the steatotic panel (C) was close to isotropic (A_4 = 0.04). The unstained vacuole-like area fraction increased from 2 % in A to 17 %, 31 % and 22 % in B, C and D. Regional analysis showed that spatial variability depended on the descriptor: GLCM contrast and energy varied by up to 12 % and 15 % between regions, whereas entropy, GLCM correlation and homogeneity were stable (coefficient of variation < 3 %). The gradient channels D1, D2 and D5 were practically redundant (Spearman $\rho \geq 0.99$). The study is intended to establish an exploratory quantitative description of the selected histological images rather than a validated classification of liver condition. Because the analysis is based on selected published image panels rather than independent biological replicates, any observed differences must be interpreted at the image level. The approach provides a structured basis for investigating multiscale and multidirectional texture organization in guppy liver histology, while highlighting the need for standardized image acquisition and independent biological validation before broader biological or diagnostic conclusions can be drawn.

Keywords: *Poecilia reticulata*, directional anisotropy, fish liver histology, histological image analysis, multiscale texture analysis, spatial heterogeneity, texture descriptors, quantitative image analysis.

Introduction. The liver is a central metabolic and detoxification organ in teleost fish and an important tissue for investigating responses to environmental contaminants. Its histological organization includes hepatocytes, vascular structures, connective tissue, and other cellular components whose appearance may change under different physiological or exposure conditions. Histopathological examination of fish liver is therefore widely used in aquatic environmental assessment, although the interpretation of tissue alterations depends on biological context, sampling, and the criteria applied to characterize lesions (Bernet et al., 1999; Wolf & Wolfe, 2005).

In *Poecilia reticulata* Peters, 1859, several investigations have examined hepatic responses to environmental contaminants and glyphosate-based herbicides. Santos et al.

(2017) reported histomorphological and protein-expression changes in the liver of female guppies exposed to a glyphosate-based herbicide. Lima-Faria et al. (2021) subsequently investigated recovery trends in guppy liver tissue following co-exposure to iron oxide nanoparticles and glyphosate. Qualhato et al. (2018) examined hepatic melanomacrophage responses and histopathological biomarkers following exposure to iron oxide nanoparticles. Together, these studies establish a species-specific basis for investigating the organization of guppy liver tissue. However, histopathological observations and molecular or cellular measurements are not equivalent to quantitative descriptions of the spatial texture of digital histological images.

The study by Martins et al. (2022) provides the biological and image-based context for the present investigation. Using histological, histochemical, and ultrastructural approaches, the authors examined liver alterations associated with co-exposure to iron oxide nanoparticles and glyphosate-based herbicides. Their observations included changes in hepatocyte morphology, steatosis, vascular disturbances, inflammatory and degenerative alterations, and changes in tissue components assessed using complementary staining procedures. The broader context is the rapid growth of engineered nanomaterials, including iron oxide nanoparticles, in biomedical and environmental applications, together with persistent questions about their characterization, biodistribution and toxicity (Goshisht et al., 2025; Jagadeesh et al., 2024; Roszkowski & Durczynska, 2025). These findings motivate a quantitative examination of the spatial patterns visible in selected liver histology images. Nevertheless, the present study does not attempt to reproduce the original toxicological experiment or infer exposure effects independently from the published panels. Its objective is to characterize image-derived properties that can be calculated using a defined texture-analysis procedure.

Conventional histological assessment remains essential for recognizing tissue architecture and identifying morphological alterations. However, visual interpretation does not necessarily provide a numerical representation of the distribution of image intensities, local transitions, directional patterns, or regional variability across a microscopic field. Quantitative texture analysis offers a complementary approach by describing spatial properties of the image through mathematically defined features. Such measurements characterize digital image patterns; their biological interpretation requires additional evidence linking the extracted features to independently established tissue characteristics. Computational analysis of histopathological images has been reviewed extensively (Gurcan et al., 2009), and the present work follows this tradition while remaining deliberately descriptive.

Several methodological approaches can be used to characterize image texture. First-order statistics describe the distribution of intensity values, whereas grey-level co-occurrence matrix (GLCM) features quantify spatial relationships between grey levels at specified offsets (Haralick et al., 1973). Gradient-based descriptors characterize local intensity transitions and their distributions, while multiscale filtering examines how image properties vary with the spatial scale of analysis. The use of Gaussian scale-space representations (Lindeberg, 1994, 1998) and of oriented derivative operators, which can be synthesized from a small set of basis filters (Freeman & Adelson, 1991), provides a mathematically controlled way of probing structure at different scales and directions. Multiscale and multidirectional biomedical texture analysis provides a framework for investigating image structure across different scales and orientations within a common analytical procedure (Depeursinge, 2017), and a hierarchical descriptor tensor that keeps scale, orientation and region as separate indices of every measurement has been formulated and verified, including on synthetic reference fields with known ground truth (Ţălu, 2027a), and applied to guppy muscle (Ţălu, 2026), to porcine and rabbit muscle (Ţălu, 2027b, 2027c) and to soil thin sections (Ţălu, 2027d). These descriptor families capture different mathematical properties and should not be assumed to provide interchangeable information. Their combined use also requires examining possible correlations and redundancy.

Scale and orientation are relevant to histological images because visible patterns may occur at different spatial extents and may exhibit preferential directions. Fine-scale

filters can respond to localized intensity transitions, whereas broader-scale filters summarize image variation over larger neighborhoods. Directional operators can reveal whether local image transitions are distributed uniformly across orientations or exhibit anisotropic organization. These responses depend on image resolution, preprocessing, filter definitions, and parameter selection. Consequently, the numerical scale of a filter must be distinguished from the physical size of a tissue structure unless image calibration is available and reliably applied.

Global measurements alone may also obscure regional differences. A single average can summarize an image while concealing local areas with distinct intensity transitions, contrast, or directional organization. Partitioning an image into regions of interest (ROIs) enables descriptor values to be examined spatially and provides a means of quantifying within-image heterogeneity. However, variation among ROIs from the same image is not equivalent to biological variation among individual fish. Regional measurements should therefore be interpreted as descriptions of spatial variability within the analyzed image rather than as independent biological replicates.

Reproducible quantitative image analysis requires explicit definitions of preprocessing, feature extraction, and measurement parameters. Differences in staining, illumination, compression, spatial resolution, cropping, grey-level discretization, and ROI selection may affect descriptor values. Standardization initiatives in quantitative imaging have demonstrated the importance of clearly defined feature calculations and reproducible computational implementations (Zwanenburg et al., 2020). These considerations are especially important when images are obtained from published figures, where the available resolution and acquisition metadata may be limited. Comparisons must consequently account for image provenance and technical differences before observed variations are attributed to tissue organization.

The present study applies a multiscale and multidirectional texture-analysis procedure to selected published liver histology images of *P. reticulata* reported by Martins et al. (2022). Ten complementary texture descriptors are evaluated at four Gaussian scales and four orientations and organized into a multidimensional descriptor tensor. Figure 1 illustrates the complete analytical chain, from the input image and its Gaussian scale-space, through oriented derivative responses and ROI aggregation, to the descriptor tensor and the derived indices reported in this paper. Global measurements and a four-region partition are used to investigate scale-dependent responses, directional anisotropy, spatial heterogeneity, and relationships among descriptors. The analysis focuses on the spatial organization represented in the selected images rather than on independently diagnosing lesions or validating the toxicological effects reported in the original study.

The objective is to determine how complementary texture descriptors characterize the selected guppy liver histology images and whether regional analysis reveals spatial variability that is not apparent from global measurements alone. The methodological contribution is the integration of scale-dependent, orientation-dependent, and region-specific measurements within a common analytical representation. Given the use of selected published image panels, the results are treated as exploratory and image-specific. Establishing biological generalizability or diagnostic value would require a larger, appropriately sampled dataset, standardized image acquisition, and validation against independent histopathological assessments.

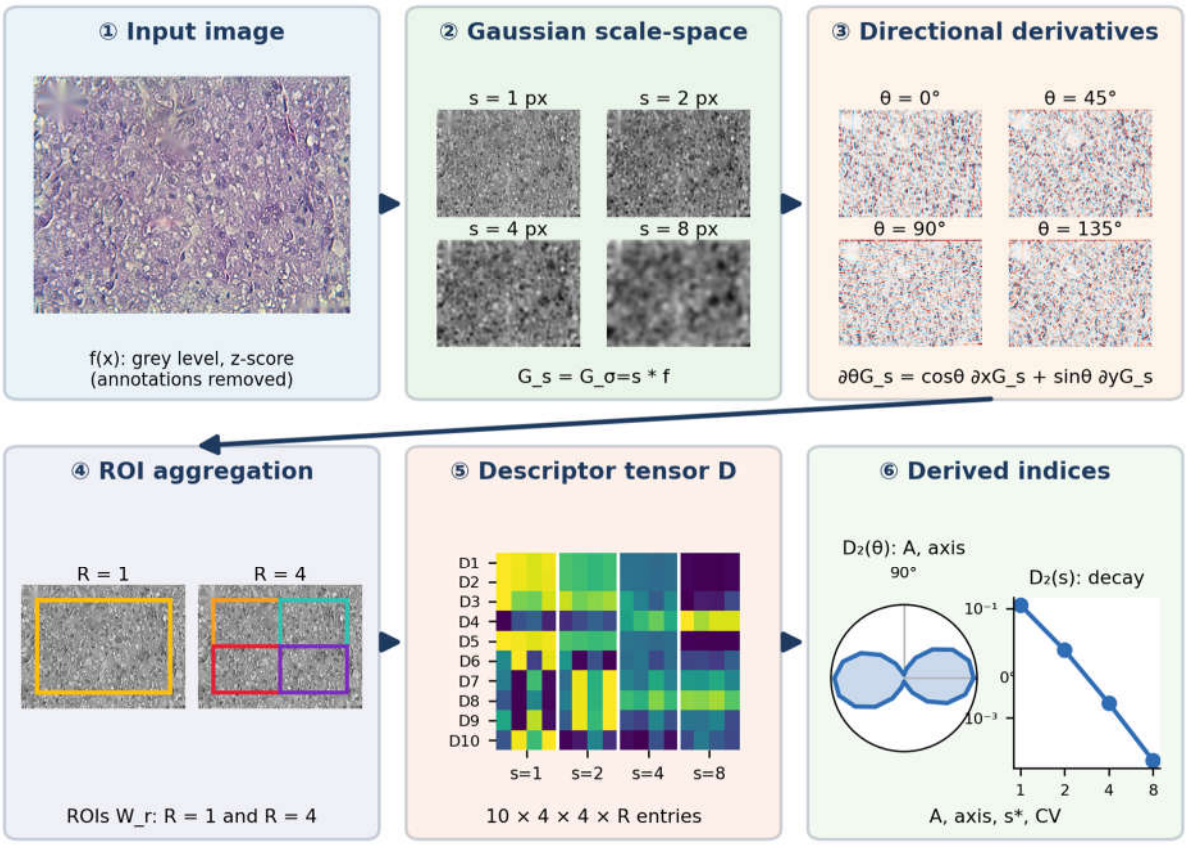


Figure 1. Schematic of the proposed hierarchical texture-characterization algorithm, illustrated with the control panel (A): ① grey-level input image after removal of annotations; ② Gaussian scale-space G_s (s = 1, 2, 4, 8 px); ③ directional derivatives $\partial\theta G_s$ at four orientations (red/blue = sign); ④ aggregation over a global ROI (R = 1) and four regional ROIs (R = 4); ⑤ descriptor tensor of 10 × 4 × 4 × R entries (heat map of the real tensor of panel A, channel-normalized); ⑥ derived indices (directional profile $D_2(\theta)$ giving the anisotropy index A and texture axis, scale decay of D_2, characteristic scale s*, and coefficient of variation across ROIs).

Material and Method

Study design and image source. This study used a computational image-analysis approach to investigate the spatial texture organization of liver histology in *Poecilia reticulata*. The analyzed material consisted of four histological image panels (A–D) from Figure 2 of Martins et al. (2022), who investigated hepatic responses to co-exposure to iron oxide nanoparticles and glyphosate-based herbicides using histological, histochemical, and ultrastructural methods. All panels show haematoxylin and eosin (HE) stained liver after 7 days of exposure; the source legend describes (A) a control group with normal arrangement of hepatocytes, (B) the FE group with large vessel congestion in the centre, (C) fat accumulation in hepatocytes of the group exposed to IONP + R2, and (D) exudate with red blood cells in the IONP + R2 group. The abbreviations FE, IONP and R2 are used as defined in the source study. In the text, panels B–D are also referred to by the appearance described in the source legend (vasocongested, steatotic, exudate); these labels describe the images, not the experimental groups. This research constitutes a secondary analysis of published images and did not involve new animal experiments, tissue sampling, or histological staining.

The panels were selected because they show four distinct tissue appearances (regular hepatocyte arrangement, vascular congestion with surrounding vacuolation, extensive steatosis, and exudate within a vessel) at the same magnification, which allows the behaviour of the descriptors to be examined across contrasting textures. The original study descriptions were used to identify the reported tissue condition and staining

method for each panel; these descriptions were retained as source metadata and were not treated as independent quantitative measurements. The image inventory, including panel identifiers, reported condition, annotation type, scale-bar information and image size, is given in Table 1. Because published figure panels may differ in resolution, cropping, compression, and display scaling, these factors were considered when assessing the comparability of the selected images.

Table 1

Image inventory of the analysed panels (Figure 2 of Martins et al. (2022))

Panel	*Condition reported in the source*	*Annotations removed*	*Crop (px)*	*Scale bar*	*µm/px*	*Inpainted share of ROI (%)*
A	Control; normal hepatocyte arrangement	arrow (microsteatosis), label, scale bar	510 × 383	≈ 83 px = 40 µm	0.485	2.0
B	FE group; large vessel congestion	star (vasocongestion), label, scale bar	510 × 383	≈ 83 px = 40 µm	0.485	1.9
C	IONP + R2; fat accumulation	arrow (macrosteatosis), label, scale bar	510 × 383	≈ 83 px = 40 µm	0.485	1.6
D	IONP + R2; exudate with RBCs	star (exudate), label, scale bar	510 × 383	≈ 83 px = 40 µm	0.485	1.2

Scale bars measured on the extracted panels: 83, 82, 83 and 83 px for 40 µm (mean 82.75 px; 0.483 µm/px). All four panels therefore share the same pixel size, which makes the pixel-based scales directly comparable across panels.

Image preparation and regions of interest. The selected image panels were extracted from the published source while preserving their available spatial resolution. No artificial enlargement was used to create additional image detail. Panel boundaries were detected from the white separators between panels and trimmed to a common size of 510 × 383 px. Annotations, arrows, stars, circular panel labels and scale bars were excluded from tissue-analysis regions because they do not represent histological structures: they were detected from their colour (near-black or saturated blue) and size, dilated by three pixels, and replaced by fast-marching inpainting (Telea, 2004) (Figure 2). The inpainted pixels amounted to 3.3–3.6 % of each panel, mostly in the corners and bottom edge outside the ROI, and to 1.2–2.0 % of the pixels inside the ROI (Table 1); the inpainted pixels were retained in the descriptor computation. Conversion to grey level used the luminance 0.299 R + 0.587 G + 0.114 B, followed by z-score normalization to zero mean and unit standard deviation over the whole panel. No contrast enhancement, sharpening or colour normalization was applied before descriptor extraction; the contrast-enhanced and colour-deconvolved renderings shown in the figures are display-only.

For the global analysis (R = 1), the ROI was the central region of each panel after removing a 48-pixel margin on every side (286 × 414 px; rows 48–333, columns 48–461). For the regional analysis (R = 4), this ROI was divided into four equal rectangles of 143 × 207 px (ROI 1 upper left, ROI 2 upper right, ROI 3 lower left, ROI 4 lower right). All filters were computed on the whole panel with reflective boundaries and descriptors were then aggregated separately in each rectangle, so that region borders do not introduce artificial edges. The four-region partition was used to examine within-image spatial heterogeneity; it was not considered a substitute for biological replication. The scale bar of each panel was measured in pixels on the extracted panel (Table 1), giving 0.483 µm per pixel; spatial scales are nevertheless reported in pixels, and the conversion to micrometres is given only as an approximate guide.

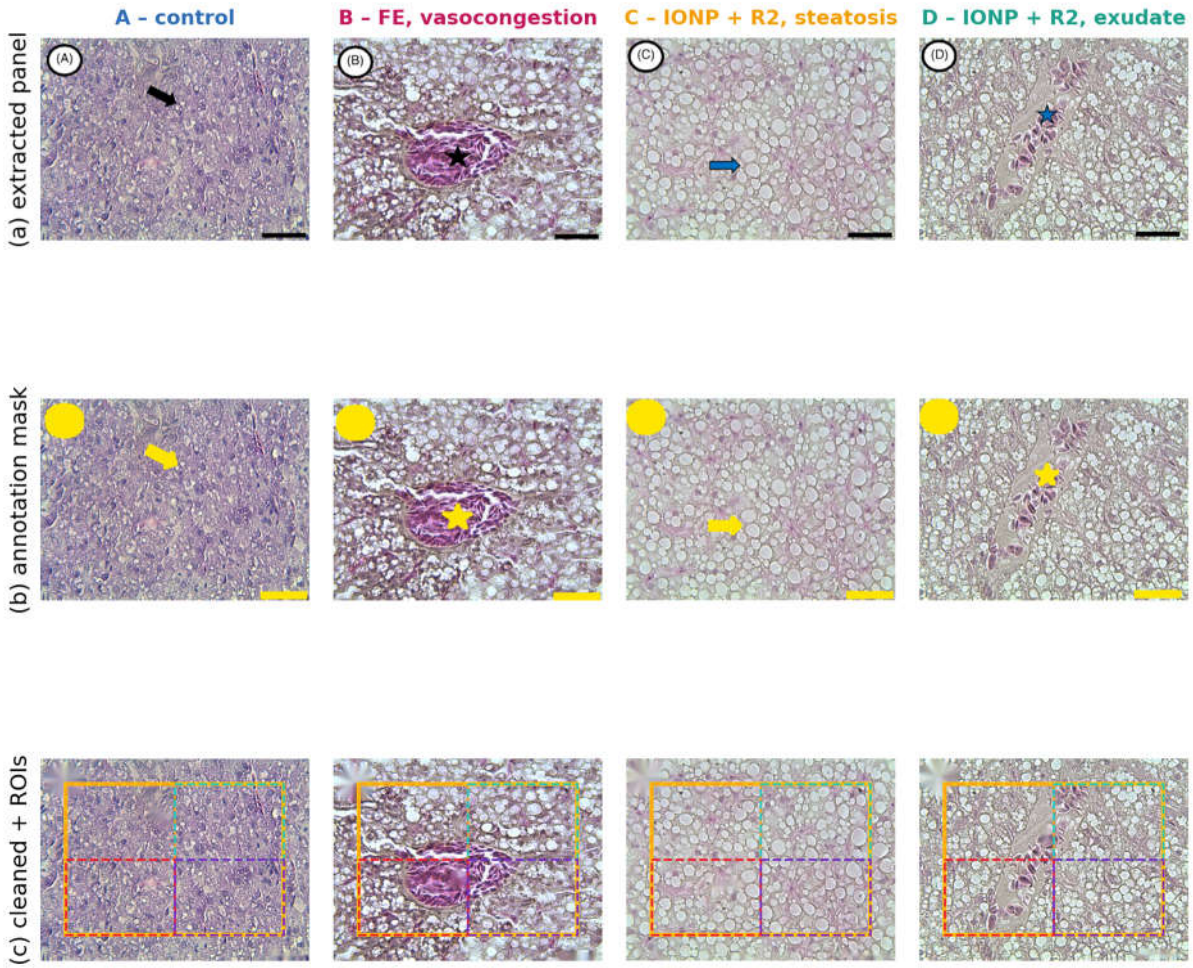


Figure 2. Extraction and cleaning of the analysed panels. (a) Panels A–D as extracted from Figure 2 of Martins et al. (2022) (Copyright License Number 6380941362622, Environmental Toxicology, 37(9), Figure 2. © 2022 John Wiley & Sons, Inc. All rights reserved), including arrows, stars, circular labels and scale bars; (b) annotation mask (yellow) used for inpainting; (c) cleaned panels with the global ROI (R = 1, solid yellow) and the four regional ROIs (R = 4, dashed colours).

Multiscale and multidirectional analysis. Texture characterization was performed using a multiscale and multidirectional procedure designed to quantify spatial variations in image intensity. Let f(x) denote the grey-level image, where x represents a pixel location in the image domain. At each selected scale, a Gaussian filtering operation $G_s = G_{\sigma=s} * f$ was used to obtain a scale-dependent representation of the image, where the scale s is the standard deviation of the Gaussian in pixels (Lindeberg, 1994, 1998). Directional measurements were evaluated at four orientations, $\theta \in \{0, \pi/4, \pi/2, 3\pi/4\}$, measured counter-clockwise from the +x axis with the y axis pointing upwards, using the first and second directional derivatives $\partial_\theta G_s = \cos\theta\, \partial_x G_s + \sin\theta\, \partial_y G_s$ and $\partial^2_\theta G_s = \cos^2\theta\, \partial_{xx} G_s + 2\sin\theta\cos\theta\, \partial_{xy} G_s + \sin^2\theta\, \partial_{yy} G_s$, which are steerable combinations of the Cartesian derivatives (Freeman & Adelson, 1991).

Four Gaussian scales, $s \in \{1, 2, 4, 8\}$ px, and four orientations were specified, and the ten descriptors (Table 3) were calculated at each scale–orientation combination. Gradient-based measurements (D1–D5) were computed over the ROI from $\partial_\theta G_s$ and $\partial^2_\theta G_s$; the entropy used 32 histogram bins over ± 4 standard deviations (bits), and the kurtosis is the Pearson kurtosis (a Gaussian distribution has kurtosis 3). GLCM-based measurements (D6–D9) were computed on G_s quantized to 16 grey levels by linear mapping over the whole panel, with offset d = s along θ rounded to integer pixels, symmetric pairing (+d and −d), normalization to a joint probability, and pairs anchored in the ROI. The autocorrelation D10 is the normalized autocovariance of G_s between a

pixel and its neighbour at lag 2s along ±θ. These implementation details are summarized in Table 2.

Table 2

Parameters and implementation of the texture-analysis procedure

Item	*Setting*
Preprocessing	Luminance (0.299 R + 0.587 G + 0.114 B); annotation removal by inpainting; z-score over the panel
Scales s	1, 2, 4, 8 px (Gaussian SD); 9 log-spaced scales (1–16 px) for the energy spectrum
Orientations θ	0, π/4, π/2, 3π/4 (0°, 45°, 90°, 135°); 12 orientations for polar profiles
Derivatives	Gaussian derivative filters, reflective boundaries; steerable combinations
ROI = 1	Central region, 48-px margin: 286 × 414 px
ROI = 4	Four equal rectangles of the central region: 143 × 207 px each
Entropy / kurtosis	32 bins over ± 4 SD, $\log_2$ (bits) / Pearson kurtosis
GLCM	16 levels (linear mapping over panel); d = s along θ rounded to pixels; ± d symmetric; ROI-anchored
Anisotropy index	A = (max − min)/(max + min) of $D_2(s, \theta)$ over θ
Texture axis	½·atan2(Σ D_2 sin 2θ, Σ D_2 cos 2θ) + 90°, in degrees from the horizontal (mod 180°)
Characteristic scale	s^* = argmax of $s^2 \cdot D_2(s)$ (mean over θ), nine log-spaced scales
Software	Python 3.12, NumPy 2.4 (Harris et al., 2020), SciPy 1.17 (Virtanen et al., 2020), scikit-image 0.26 (van der Walt et al., 2014), OpenCV 4.13 (Bradski, 2000), Matplotlib 3.10 (Hunter, 2007)

Table 3

The ten descriptor channels of the tensor

Channel	*Definition*	*Family*
D1	mean of $\lvert\partial_\theta G_s\rvert$	gradient-based
D2	energy: mean of $(\partial_\theta G_s)^2$	gradient / filter-based
D3	kurtosis of $\partial_\theta G_s$	gradient statistics
D4	Shannon entropy of $\partial_\theta G_s$ (32 bins, ± 4 SD, bits)	gradient statistics
D5	mean of $\lvert\partial^2_\theta G_s\rvert$ (second derivative)	filter-based
D6	GLCM contrast	statistical / spatial dependence
D7	GLCM homogeneity	statistical / spatial dependence
D8	GLCM energy (angular second moment)	statistical / spatial dependence
D9	GLCM correlation	statistical / spatial dependence
D10	normalized autocorrelation of G_s at lag 2s along θ	spatial dependence

Descriptor tensor and global measurements. Texture descriptors were organized according to the hierarchical representation of the descriptor tensor. Let $D_m(s, \theta, W)$ denote the value of descriptor m, evaluated at spatial scale s, orientation θ, and spatial support W. This parameterization distinguishes the mathematical definition of each descriptor from the scale, directional configuration, and spatial domain used for its evaluation. For the present analysis, the descriptor set comprised M = 10 channels, evaluated at K = 4 scales, $s_k \in \{1, 2, 4, 8\}$, and L = 4 orientations. The resulting measurements were organized into a descriptor tensor indexed by descriptor, scale, orientation, and region of interest:

$$\mathfrak{D} \in \mathbb{R}^{M \times K \times L \times R} \quad (1)$$

with individual entries defined as

$$\mathfrak{D}_{mklr} = D_m(s_k, \theta_l, W_r) \quad (2)$$

where m = 1,…, M, k = 1,…, K, l = 1,…, L, and r = 1,…, R. Here, W_r denotes the spatial support associated with region r, and R is the number of regions included in the corresponding tensor. For the whole-image analysis, R = 1, yielding 10 × 4 × 4 × 1 = 160 descriptor entries per panel. For the regional analysis, the image was partitioned into four regions, yielding 10 × 4 × 4 × 4 = 640 entries per panel; all 160 + 640 entries of the four panels (3,200 values) are provided as Supplementary Table S1. Whole-image and regional representations were retained as distinct analytical configurations so that global measurements could be distinguished from within-image spatial variability.

Descriptor computation, normalization, and regional aggregation were treated as separate operations. Global measurements were used to characterize the overall image response at each scale and orientation, whereas regional measurements were used to examine the spatial distribution of descriptor values. Variations across scales characterized scale-dependent responses, and variations across orientations characterized directional sensitivity. The tensor provides a structured representation of the selected image-derived measurements; its dimensionality is determined by the number of descriptors and the sampling configuration. It does not imply statistical independence among descriptors, biological replication among image regions, or validated diagnostic performance. Accordingly, the tensor was used to organize and compare the texture properties of the analyzed liver histology images rather than to infer population-level biological effects.

Regional heterogeneity and descriptor relationships. Regional heterogeneity was examined by calculating the selected descriptors separately within each of the four ROIs. For each descriptor, the regional mean, standard deviation, and coefficient of variation (CV; the ratio of the standard deviation to the mean, in percent) were calculated at $s = 2$ px after averaging over the four orientations. The CV was interpreted only when the mean was sufficiently different from zero. Because all four regions originated from the same panel, they were treated as subsamples for spatial characterization rather than as independent biological observations, and no population-level statistical inference was made from regional measurements.

Relationships among descriptors were examined using Spearman rank correlation (Spearman, 1904) over all $n = 256$ tensor entries of the $R = 4$ configuration (4 panels × 4 scales × 4 orientations × 4 ROIs for each channel). Correlations were interpreted as evidence of statistical association within the analyzed data, not as proof that two descriptors are mathematically equivalent or biologically interchangeable. As an exploratory summary, the mean-over-θ values of eight non-redundant channels at four scales (32 features) were log-transformed where appropriate, z-scored across panels, and compared by Euclidean distance and principal component analysis; with only four panels this summary is purely descriptive.

Complementary renderings and morphometric cross-check. To make the tissue patterns visible beyond a single bright-field rendering, each panel was also displayed (i) after contrast-limited adaptive histogram equalization of the lightness channel (Zuiderveld, 1994), (ii) as the gradient-magnitude map at $s = 2$ px, (iii) as haematoxylin and eosin optical-density channels obtained by colour deconvolution (Macenko et al., 2009; Ruifrok & Johnston, 2001), (iv) as directional derivative maps, and (v) as local orientation and coherence maps computed from the same oriented derivatives (smoothing $\sigma = 8$ px). These renderings are used only for visualization; all descriptors were computed on the unprocessed (cleaned, z-scored) grey-level image.

As an independent cross-check of the tensor, unstained vacuole-like regions (lipid vacuoles and lumina) were delineated by fixed thresholds on the HSV representation (value > 0.80 and saturation < 0.14), followed by a one-pixel opening; objects of at least 20 pixels that did not touch the ROI border were retained, and their equivalent circular diameter was calculated with the scale-bar calibration. This segmentation is approximate (touching vacuoles may merge and the thresholds were fixed rather than tuned per panel) and was used only to relate the texture results to a simple morphometric quantity.

Image comparability and methodological limitations. Image comparability was assessed with respect to staining, tissue condition as described in the source, image dimensions, available resolution, cropping, and scale-bar information. Because the images were obtained from published figure panels, the analysis was potentially affected by image compression, figure-layout processing, and the absence of original microscope files. These limitations were considered when interpreting differences in descriptor values. The study was designed as an exploratory image-analysis investigation. Published panels do not necessarily represent independent fish, and multiple ROIs extracted from

one panel cannot be counted as independent biological replicates. Accordingly, the analysis was limited to the quantitative description of the selected images. It was not designed to estimate population-level effects, validate a diagnostic classifier, or establish a causal relationship between exposure and texture changes. The source of each analyzed image is the publication of Martins et al. (2022), © 2022 Wiley Periodicals LLC. That article is not open access; reproduction of its Figure 2 panels (Figure 2a of this paper) and of renderings derived from them (Figures 1–5, 7, 9, 13 and 14) requires permission from the publisher, which is requested through the Copyright Clearance Center service for reuse in a journal article (see the Copyright and permissions statement).

Descriptive statistics were used to summarize global and regional descriptor values, and correlation analysis was used to examine relationships among descriptors. Given the exploratory design and the use of selected published images, inferential statistical tests were not used to claim biological differences between exposure conditions. Numerical comparisons were interpreted as differences between the analyzed image panels.

Theoretical basis of the derived indices. The descriptor tensor and its reference implementation were introduced, and verified on synthetic reference fields, by Ţălu (2027a). This section states, in a form adapted to histological panels with heterogeneous content, the properties of the tensor that are used to interpret the results. Notation follows Section 2.3: $G_s = g_s * f$ is the Gaussian-smoothed, z-scored image, $\mathbf{u}_\theta = (\cos\theta, \sin\theta)^{\mathrm{T}}$, and $\langle\cdot\rangle_r$ is the mean over the region W_r.

Channels as functionals of a distribution. For each (s, θ, r), let $\mu_{s,\theta,r}$ be the distribution of the directional derivative $\partial_\theta G_s$ over the pixels of W_r. Channels D1–D4 are functionals of this single distribution,

$$D_1 = \int |v|\, d\mu, \quad D_2 = \int v^2\, d\mu, \quad D_3 = \frac{\int (v-\bar{v})^4 d\mu}{\left(\int (v-\bar{v})^2 d\mu\right)^2}, \quad D_4 = -\sum_b p_b \log_2 p_b \qquad (3)$$

where p_b are the masses of μ in the 32 standardized bins, and D5 is the analogous first absolute moment of the second derivative. Two invariances follow and matter for published panels whose staining and illumination differ. Because f is z-scored, every channel is invariant to an affine change of grey level, $f \mapsto af + b$ with $a > 0$. Because D3 and D4 are computed after standardizing $\partial_\theta G_s$, they are additionally invariant to the amplitude of the gradient and describe only the *shape* of its distribution (heavy tails, spread). Non-affine differences in staining are not removed by either operation; they change the distribution μ and, through the quantization, the co-occurrence channels D6–D9. The ratios of Table 8 therefore compare functionals of μ between panels after affine normalization, not raw intensities.

Directional energy, anisotropy index and texture axis. Let $\mathbf{J}_{s,r} = \langle \nabla G_s \nabla G_s^{\mathrm{T}} \rangle_r$ with eigenvalues $\lambda_+ \geq \lambda_-$. As shown in that study, $D_2(s,\theta,r) = \mathbf{u}_\theta^{\mathrm{T}} \mathbf{J}_{s,r} \mathbf{u}_\theta$, so that the four tensor orientations determine $\mathbf{J}_{s,r}$ exactly ($J_{xx} = D_2(0)$, $J_{yy} = D_2(\pi/2)$, $J_{xy} = 1/2\,[D_2(\pi/4) - D_2(3\pi/4)]$), and

$$A = \frac{\lambda_+ - \lambda_-}{\lambda_+ + \lambda_-} = \frac{|\langle z_s \rangle_r|}{\langle |z_s| \rangle_r}, \qquad z_s = \left(\partial_x G_s + i\, \partial_y G_s\right)^2 \qquad (4)$$

i.e. A is the energy-weighted mean resultant length of the doubled gradient directions (Bigün & Granlund, 1987; Mardia & Jupp, 2000). The index reported in Tables 6, 11, 12 and 16 is computed from the four sampled orientations, $A_4 = (\max_l D_2 - \min_l D_2)/(\max_l D_2 + \min_l D_2)$. Since $D_2(\theta)$ varies as $\cos 2(\theta - \varphi)$ and every direction lies within $\pi/8$ of a sampled orientation,

$$A/\sqrt{2} \leq A_4 \leq A \qquad (5)$$

with $A_4 = A$ when the texture axis coincides with a sampled orientation. A_4 is therefore a conservative estimate of directional organization; for brevity it is denoted A in those tables and in the text, and the index computed from the structure matrix is reported separately in Table 17. The texture axis ψ = φ + π/2 (mod π), where φ is the direction of the leading eigenvector of the structure matrix, is the direction along which

the dominant intensity boundaries run, perpendicular to the dominant gradient direction; it is computed from all four entries and is exact for D_2.

Dilution by isotropic structure. Suppose that the gradient energy in a region is the sum of an oriented component with structure matrix $\mathbf{J}_a$ (anisotropy A_a, energy $E_a = \mathrm{tr}\mathbf{J}_a$) and an isotropic component whose structure matrix is $1/2\, E_{\mathrm{iso}}\mathbf{I}$, the cross terms averaging to zero. Then $\lambda_+ - \lambda_-$ is unchanged and the trace increases, so

$$A = A_a \frac{E_a}{E_a + E_{\mathrm{iso}}} \qquad (6)$$

Rounded objects whose boundaries take all orientations, such as lipid vacuoles, contribute an approximately isotropic component. Eq. (6) predicts that, other things being equal, an increase of the share of gradient energy produced by vacuole rims lowers the anisotropy index of the parenchyma in proportion to that share, without any change in the orientation of the remaining structures.

Regional aggregation. For channels defined as regional means (D1, D2, D5 and the entries of $\mathbf{J}$), the value for a union of equal-area regions is the mean of the regional values; this identity underlies the consistency check of Table 13. The anisotropy index is not additive: for an equal-area partition of the global ROI into regions with indices A_r and energies E_r,

$$A(\mathrm{global}) \le \frac{\sum_r E_r A_r}{\sum_r E_r} \qquad (7)$$

with equality if and only if the regional texture axes coincide (Ţălu, 2027a). The gap between the two sides of Eq. (7) measures how much directional organization is lost by summarizing a heterogeneous panel with one number.

Physical scale. For a pixel size Δ, the Gaussian scale s px corresponds to $s\Delta$ µm, and the tensor of an image resampled by a factor c at scale s equals that of the original image at scale cs (up to a factor c^2 for energy-type channels) (Ţălu, 2026). With $\Delta = 0.483$ µm/px (Table 1), the scales $s = 1$–8 px probe structures of about 0.5–3.9 µm, smaller than a hepatocyte or a large vacuole; this bound is used in the interpretation of Section 3.4.

Results and Discussion

Global intensity and colour summary

Table 4

First-order statistics of the luminance (0–255) inside the global ROI, mean colour saturation, and unstained-area fraction

Panel	*Mean*	*SD*	*Skewness*	*Kurtosis*	*Mean saturation (%)*	*Unstained area (%)*
A	153.8	35.7	0.26	3.13	18.7	2.0
B	160.6	52.9	0.03	2.10	19.0	17.5
C	185.1	29.8	−0.32	2.84	7.7	31.1
D	179.2	41.6	−0.07	2.35	10.1	22.1

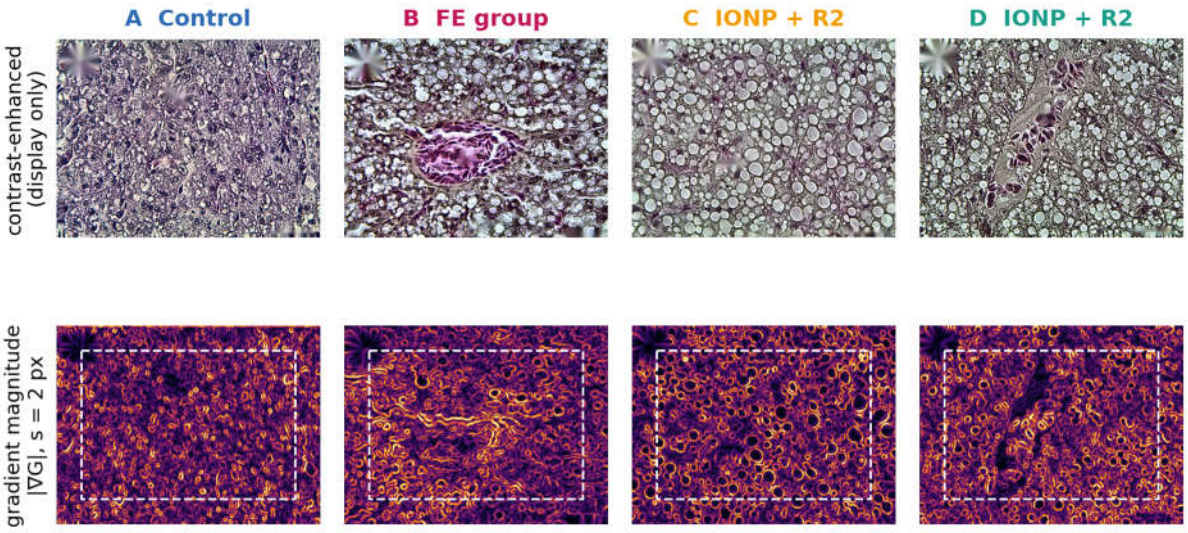


Figure 3. Alternative renderings of the cleaned panels. Top: contrast-limited adaptive histogram equalization (display only). Bottom: gradient-magnitude map |∇G| at s = 2 px (dashed line: global ROI).

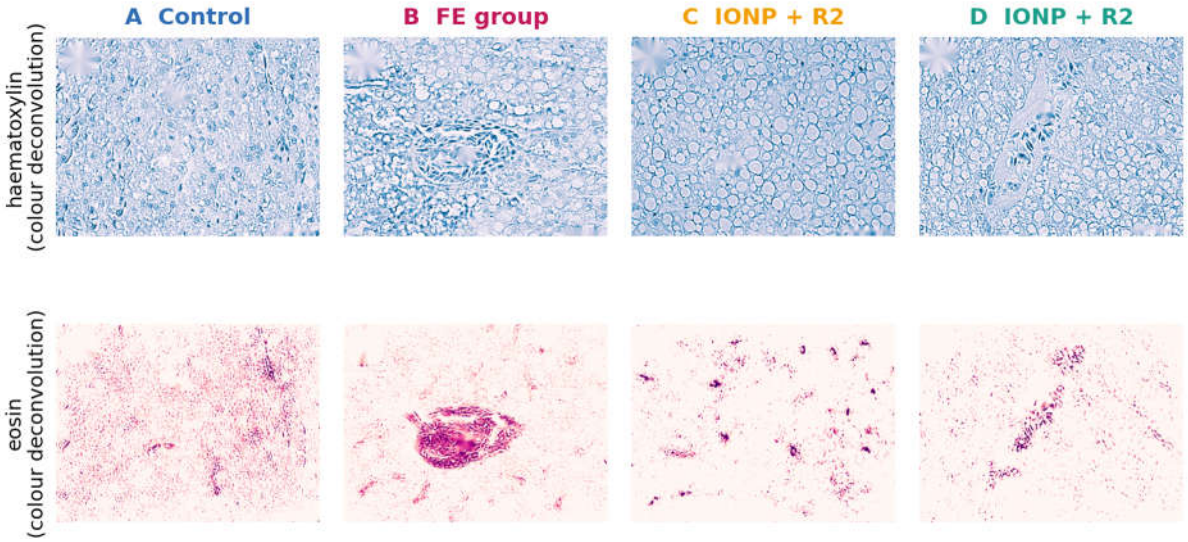


Figure 4. Colour-deconvolved haematoxylin (top) and eosin (bottom) optical-density channels of the four panels (display only).

Interpretation. The four panels differ clearly in global intensity statistics. Panel A is the darkest (mean luminance 154) and, together with B, the most saturated (mean saturation ≈ 19 %), whereas the vacuolated panels C and D are paler (mean luminance 185 and 179) and less saturated (8 % and 10 %). Panel B has the widest luminance distribution (SD 52.9) and the lowest kurtosis (2.10), consistent with the coexistence of very bright vacuoles and a dark, eosinophilic vessel; panel C has the narrowest distribution (SD 29.8) and a negative skewness (−0.32). These global values describe intensity only and cannot distinguish a regular arrangement of cells from, for example, a regular arrangement of vacuoles, which motivates the spatial descriptors below. The gradient-magnitude maps (Figure 3) show dense, fine edges in A, a strong boundary around the vessel in B, and ring-like boundaries around vacuoles in C and D; the deconvolved channels (Figure 4) show haematoxylin-stained nuclei distributed throughout A and as a dense cluster around the vessel in B, whereas eosin is concentrated in the vessel contents of B and in the red-cell cluster of D, with little eosin signal elsewhere.

Directional responses and the descriptor tensor

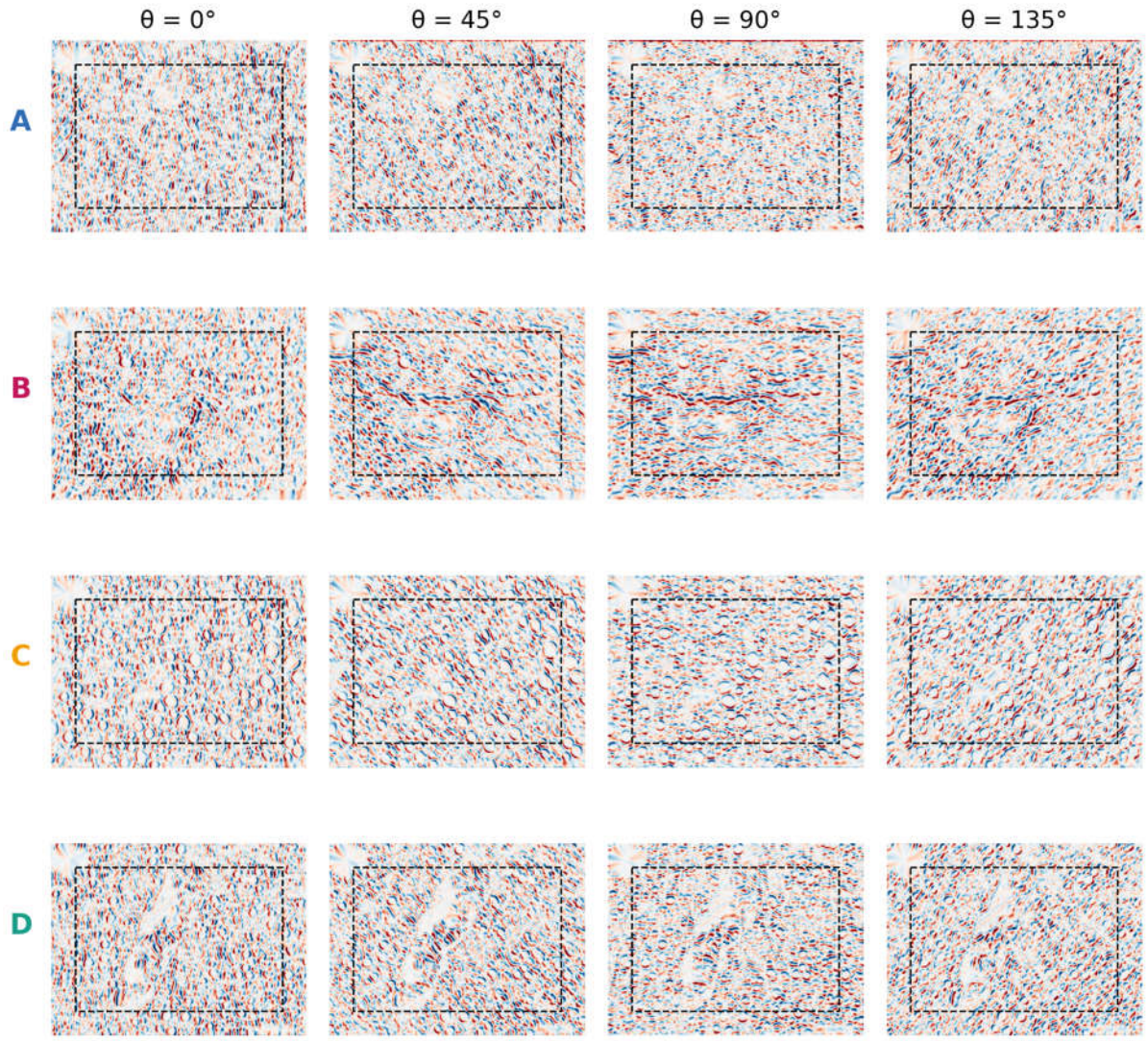


Figure 5. Directional derivative ∂θG at s = 2 px for the four orientations in panels A–D (red/blue = sign; dashed line: global ROI).

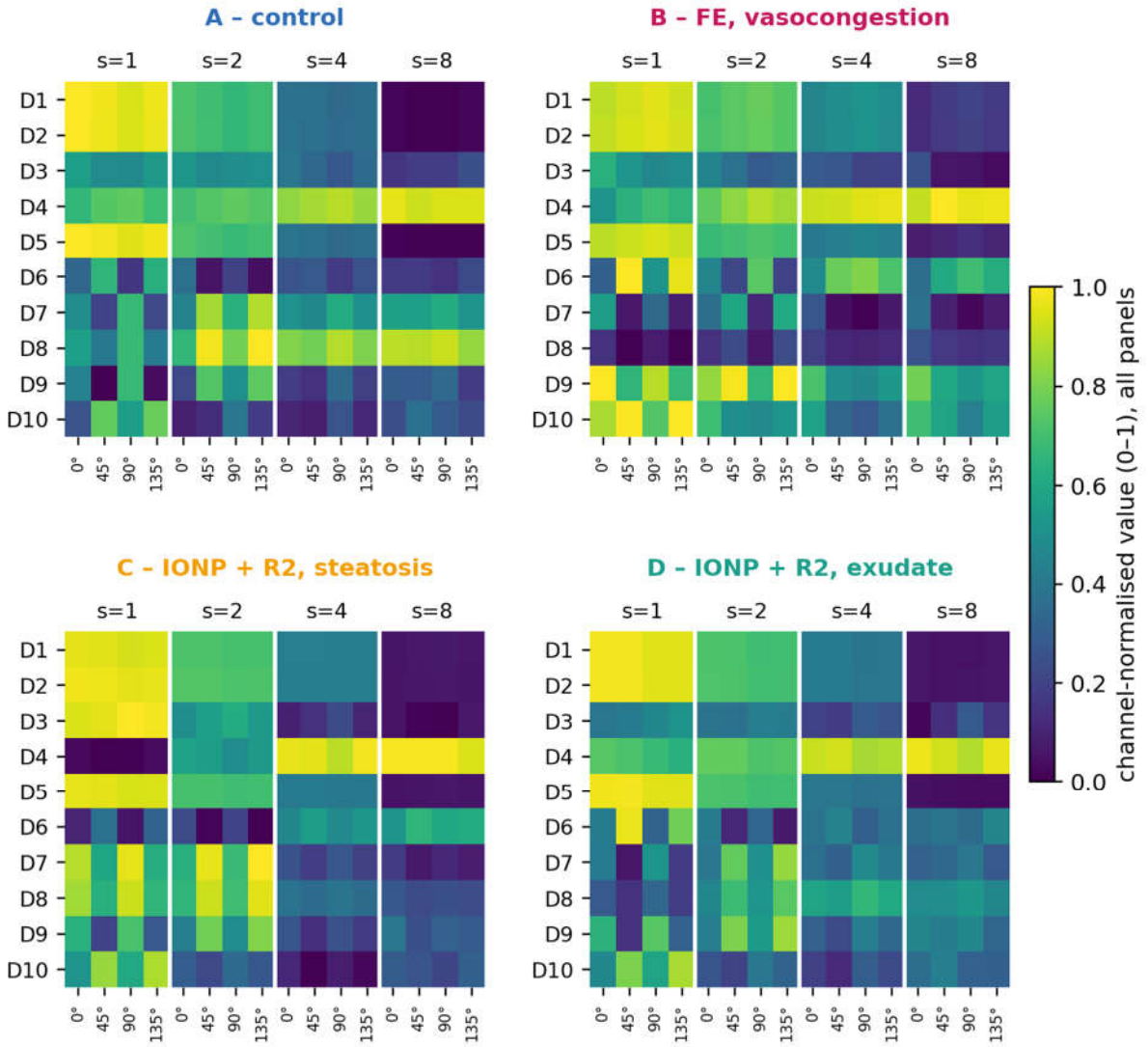


Figure 6. Descriptor tensor for R = 1: channel-normalized values (0–1; logarithmic scale for D1, D2 and D5) of the ten channels at four scales and four orientations for each panel.

Table 5

Mean-over-θ values of the ten descriptors at each scale for the four panels (global ROI, 3 significant digits). Shading increases with the value within each row

Channel	*Scale*	*A – control*	*B – FE group*	*C – IONP + R2 (steatosis)*	*D – IONP + R2 (exudate)*
D1	s = 1	0.257	0.222	0.236	0.25
	s = 2	0.0995	0.118	0.108	0.105
	s = 4	0.0334	0.0508	0.0422	0.0379
	s = 8	0.0102	0.0174	0.0123	0.012
D2	s = 1	0.117	0.0899	0.113	0.113
	s = 2	0.0174	0.024	0.0215	0.0197
	s = 4	0.00187	0.00426	0.0029	0.00244
	s = 8	0.000168	0.000483	0.000236	0.000232
D3	s = 1	4.15	4.19	5.3	3.98
	s = 2	4.12	3.76	4.25	3.88
	s = 4	3.71	3.47	3.22	3.44
	s = 8	3.34	3.11	2.94	3.23
D4	s = 1	4.01	4	3.92	4.01
	s = 2	4.01	4.03	3.99	4.01
	s = 4	4.03	4.04	4.04	4.04
	s = 8	4.04	4.04	4.05	4.04
D5	s = 1	0.233	0.171	0.199	0.219
	s = 2	0.0537	0.0535	0.0545	0.0552
	s = 4	0.0094	0.0131	0.0117	0.0106
	s = 8	0.00143	0.00243	0.00187	0.00168

Channel	*Scale*	*A – control*	*B – FE group*	*C – IONP + R2 (steatosis)*	*D – IONP + R2 (exudate)*
D6	s = 1	1.43	1.92	0.98	1.78
	s = 2	0.887	1.35	0.791	1.02
	s = 4	1.04	1.91	1.55	1.3
	s = 8	0.919	1.68	1.72	1.32
D7	s = 1	0.663	0.637	0.733	0.642
	s = 2	0.722	0.666	0.743	0.706
	s = 4	0.687	0.605	0.629	0.661
	s = 8	0.695	0.613	0.607	0.65
D8	s = 1	0.0414	0.0192	0.0536	0.0277
	s = 2	0.0579	0.0245	0.0555	0.0455
	s = 4	0.0563	0.0228	0.0342	0.0455
	s = 8	0.0594	0.0252	0.0284	0.0401
D9	s = 1	0.821	0.912	0.851	0.851
	s = 2	0.867	0.924	0.881	0.886
	s = 4	0.807	0.867	0.806	0.827
	s = 8	0.818	0.88	0.824	0.843
D10	s = 1	0.709	0.85	0.765	0.751
	s = 2	0.533	0.69	0.573	0.578
	s = 4	0.507	0.619	0.468	0.539
	s = 8	0.57	0.7	0.565	0.603

Interpretation. All gradient-based channels (D1, D2, D5) decrease steeply with scale, as expected for smoothing. At s = 2 px the energy D_2 is highest in panel B (0.024) and lowest in the control A (0.0174); at s = 4 px panel B exceeds A by a factor of 2.3, indicating that a larger fraction of its gradient energy lies at coarser scales, as would be expected from the vessel boundary and large vacuoles. GLCM contrast (D6) is highest in B (1.35 at s = 2 px; 1.91 at s = 4 px) and GLCM energy (D8) is lowest in B (0.025), while the control A and the steatotic panel C have almost identical D8 at s = 2 px (0.058 and 0.055). The entropy D4 is practically constant across panels and scales (≈ 4.0 bits) and therefore does not discriminate these images. The autocorrelation D10 is markedly higher in B (0.69 at s = 2 px versus 0.53–0.58 in the others), reflecting long-range correlation in the vessel region.

Directional organization and anisotropy

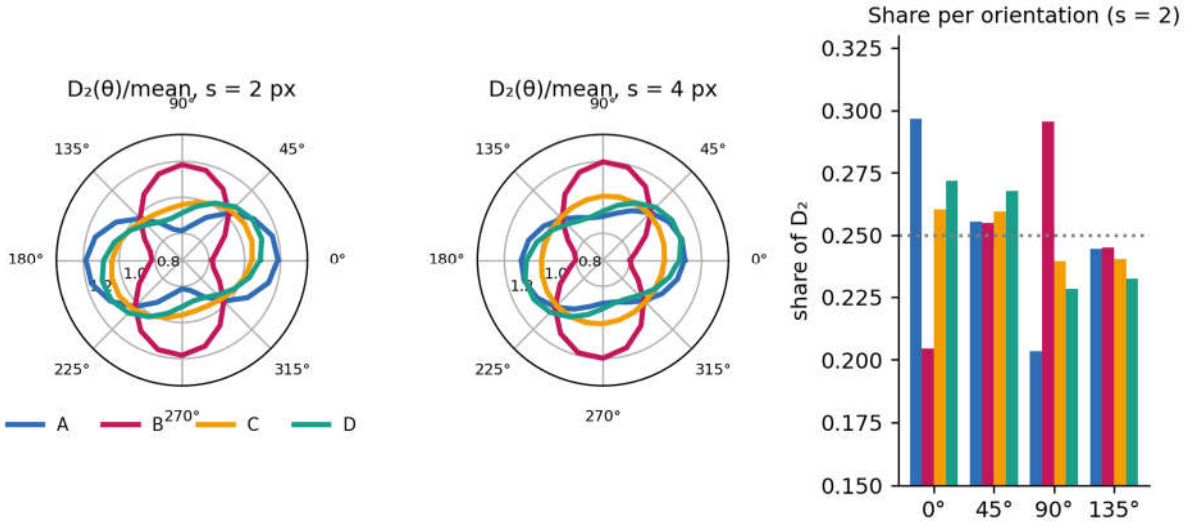


Figure 7. Directional energy profiles. Polar plots of $D_2(\theta)$ normalized to its mean over θ (12 orientations) at s = 2 px and s = 4 px, and share of D_2 energy at the four tensor orientations (s = 2 px; dotted line: isotropic share 0.25).

Table 6

D_2 energy share per orientation, anisotropy index A and texture axis for the global ROI (axis in degrees counter-clockwise from the horizontal)

Scale	*Panel*	*θ = 0°*	*θ = 45°*	*θ = 90°*	*θ = 135°*	*A*	*Texture axis*
s = 1	A	0.298	0.254	0.202	0.246	0.191	92°
	B	0.207	0.254	0.293	0.246	0.171	178°
	C	0.269	0.261	0.231	0.239	0.076	105°
	D	0.273	0.273	0.227	0.227	0.092	112°
s = 2	A	0.297	0.255	0.203	0.245	0.186	93°
	B	0.204	0.255	0.296	0.245	0.182	177°
	C	0.260	0.260	0.240	0.240	0.041	112°
	D	0.272	0.268	0.228	0.232	0.087	110°
s = 4	A	0.277	0.256	0.223	0.244	0.107	97°
	B	0.201	0.257	0.299	0.243	0.198	176°
	C	0.248	0.254	0.252	0.246	0.015	148°
	D	0.269	0.266	0.231	0.234	0.077	110°
s = 8	A	0.259	0.236	0.241	0.264	0.058	61°
	B	0.193	0.250	0.307	0.250	0.229	0°
	C	0.236	0.256	0.264	0.244	0.054	169°
	D	0.253	0.239	0.247	0.261	0.046	53°

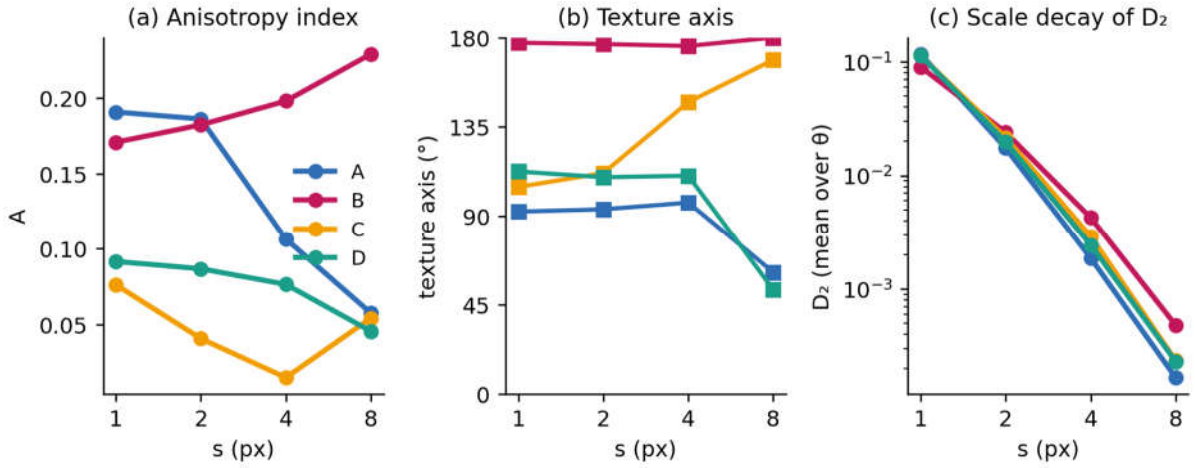


Figure 8. (a) Anisotropy index A, (b) texture axis and (c) scale decay of D_2 as functions of the Gaussian scale for panels A–D (axis values near 0° and 180° are equivalent).

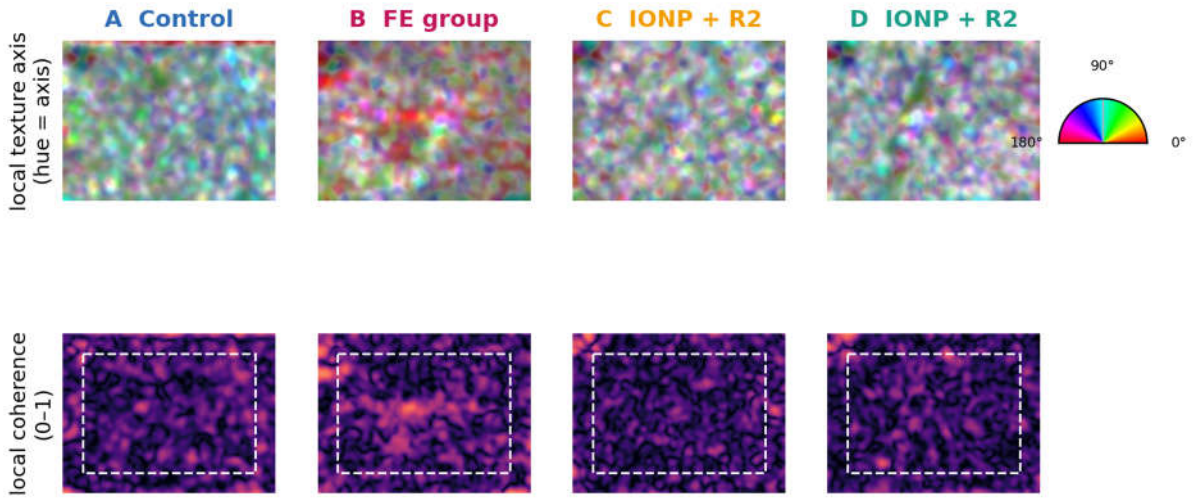


Figure 9. Local texture-orientation maps (hue = local axis, brightness = energy) and local coherence (0–1) computed from the same oriented derivatives at s = 2 px (σ = 8 px smoothing). Complementary illustration, not a tensor entry.

Interpretation. The panels differ in their directional organization. Panel A shows moderate anisotropy at fine scales (A = 0.19 at s = 1 px and 0.19 at s = 2 px) with a texture axis near 93° (vertical), which decreases to 0.06 at s = 8 px. Panel B shows a horizontal axis (177° at s = 2 px) whose anisotropy increases with scale (A = 0.17 → 0.23), as expected when the elongated vessel and its boundary dominate the coarse scales. The steatotic panel C is the least oriented (A = 0.041 at s = 2 px, 0.015 at s = 4 px) and its axis is not stable across scales (from 105° to 169°), the expected behaviour of a nearly isotropic field of rounded vacuoles. Panel D is weakly anisotropic (A ≈ 0.09) with an axis near 110°. Values of A below about 0.05 should be regarded as close to the isotropy floor for such ROIs (isotropic surrogates were not computed here; in the guppy muscle panels analysed with the same tensor the surrogate 95th percentile did not exceed 0.034 (Ţălu, 2026), so 0.05 is a conservative threshold); consequently, the axes reported for panel C at s ≥ 4 px, and for A and D at s = 8 px, are not meaningful. The local maps (Figure 9) are consistent with this picture: local orientations are largely random in C and D, whereas B shows a coherent region around the vessel.

Scale behaviour

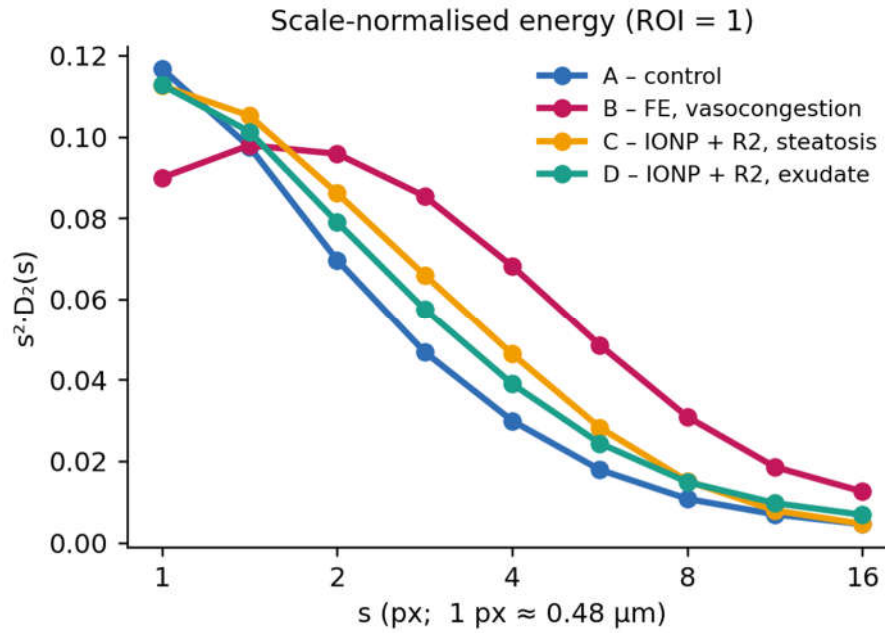


Figure 10. Scale-normalized energy $s^2 \cdot D_2(s)$ (mean over θ; global ROI) at nine log-spaced scales.

Table 7

Scale-normalized energy $s^2 \cdot D_2(s)$ (mean over θ) at nine log-spaced scales, its maximum, and the log–log slope of D_2 against s

s (px)	*s (µm)*	*A – control*	*B – FE group*	*C – IONP + R2*	*D – IONP + R2*
1.00	0.5	0.1167	0.0899	0.1126	0.1127
1.41	0.7	0.0975	0.0979	0.1052	0.1012
2.00	1.0	0.0697	0.0958	0.0861	0.0790
2.83	1.4	0.0468	0.0854	0.0660	0.0575
4.00	1.9	0.0299	0.0682	0.0463	0.0390
5.66	2.7	0.0179	0.0486	0.0282	0.0244
8.00	3.9	0.0107	0.0309	0.0151	0.0149
11.31	5.5	0.0069	0.0186	0.0079	0.0097
16.00	7.8	0.0045	0.0125	0.0046	0.0068
Argmax s* (px)		1.00	1.41	1.00	1.00
Decay exponent of D_2 (log–log slope, s = 1–8)		−3.15	−2.51	−2.96	−2.98

Interpretation. For panels A, C and D, the normalized energy decreases monotonically from the finest scale (s* = 1.0 px ≈ 0.5 µm), i.e. no characteristic scale is detected inside 1–16 px; at this resolution the dominant gradient energy comes from the sharpest boundaries (membranes, vacuole rims, nuclear edges) and from image noise and compression. Panel B differs: its normalized energy has a broad plateau between s = 1.4 and 2.8 px with a maximum at s* = 1.41 px (≈ 0.7 µm), and its D_2 decays more slowly with scale (log–log slope −2.51 versus −3.15 to −2.98 for the other panels). More energy at intermediate-to-coarse scales in B is consistent with the presence of a large structure (the vessel with its wall) in addition to small vacuoles. The absence of a clear scale peak in the vacuolated panels C and D should not be read as an absence of vacuoles: vacuole diameters (Section 3.7) are 3–9 µm, i.e. 6–18 px, but their boundaries are sharp and generate gradient energy at all scales, which a single normalized-energy maximum does not resolve. In physical units (Section 2.8), the tested scales (0.5–3.9 µm) lie below the vacuole diameters, so the scale set probes vacuole rims and membranes rather than whole vacuoles.

Comparison of descriptors with the control panel

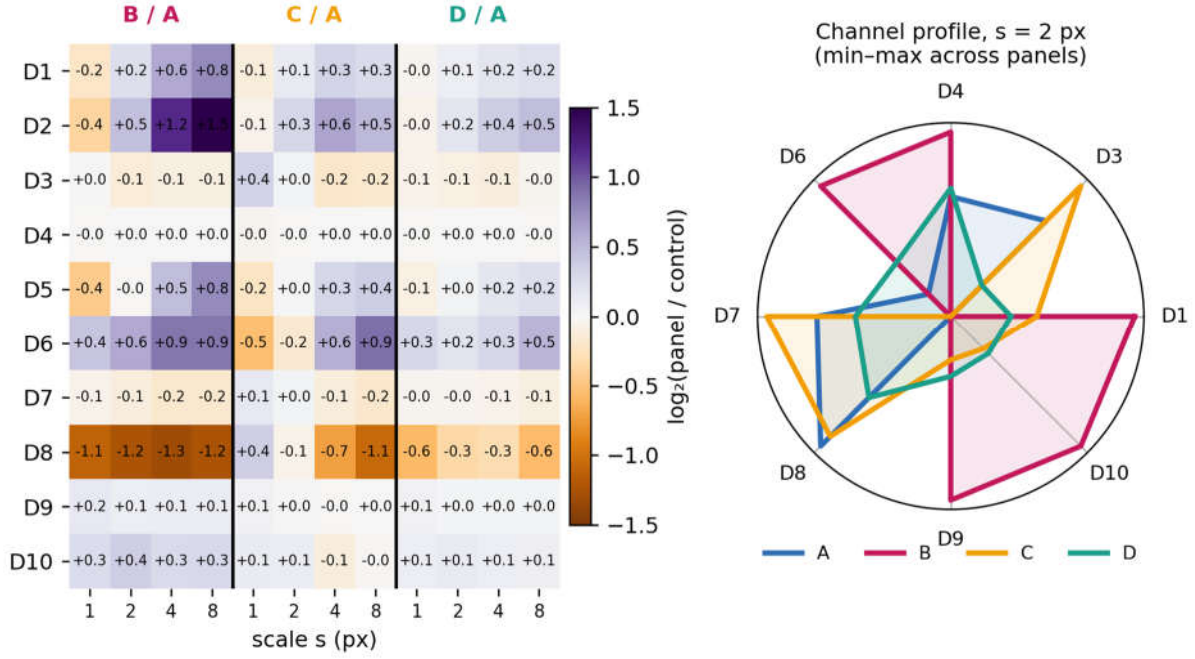


Figure 11. (Left) $\log_2$ ratio of each descriptor (mean over θ) in panels B, C and D relative to the control panel A, for the four scales. (Right) Channel profile at s = 2 px for the eight non-redundant channels, min–max normalized across panels.

Table 8

Ratio of each descriptor (mean over θ) to the control panel A at s = 2 and s = 4 px (orange: lower than A; purple: higher than A)

Channel	*Descriptor*	*B/A s=2*	*C/A s=2*	*D/A s=2*	*B/A s=4*	*C/A s=4*	*D/A s=4*
D1	Mean $\lvert\partial\theta G\rvert$	1.18	1.09	1.06	1.52	1.26	1.14
D2	Energy $(\partial\theta G)^2$	1.38	1.24	1.13	2.28	1.55	1.30
D3	Kurtosis of ∂θG	0.91	1.03	0.94	0.93	0.87	0.93
D4	Entropy of ∂θG (bits)	1.00	0.99	1.00	1.00	1.00	1.00
D5	Mean $\lvert\partial^2\theta G\rvert$	1.00	1.01	1.03	1.39	1.24	1.12
D6	GLCM contrast	1.52	0.89	1.15	1.83	1.49	1.24
D7	GLCM homogeneity	0.92	1.03	0.98	0.88	0.92	0.96
D8	GLCM energy	0.42	0.96	0.79	0.40	0.61	0.81
D9	GLCM correlation	1.07	1.02	1.02	1.07	1.00	1.02
D10	Autocorrelation (lag 2s)	1.29	1.07	1.09	1.22	0.92	1.06

Interpretation. Relative to A, the vasocongested panel B shows the largest departures: higher gradient energy at coarse scales (D2 ratio 2.28 at s = 4 px), higher GLCM contrast (1.52 at s = 2 px) and autocorrelation, and lower GLCM energy (0.42). The steatotic panel C departs mainly in the GLCM-contrast and kurtosis channels at s = 2 px (D6 ratio 0.89, D3 ratio 1.03), and panel D is intermediate and closest to A overall. Importantly, several descriptors do not separate A from the strongly vacuolated panel C at the finest scales (e.g. D4, D7, D9 and D8 at s = 2 px are within about 5 % of A), showing that global texture descriptors and tissue pathology are not interchangeable and that a visually obvious change (31 % unstained area in C versus 2 % in A) may leave several descriptors almost unchanged.

Directional modulation of the channels

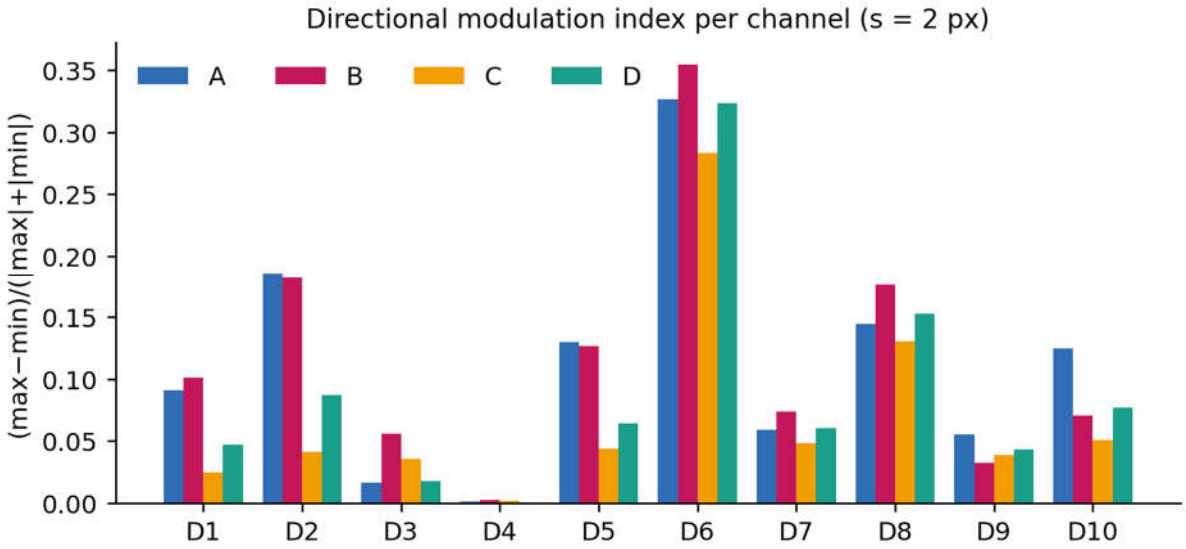


Figure 12. Directional modulation index of each descriptor at s = 2 px for panels A–D.

Table 9

Directional modulation index (max − min)/(|max| + |min|) of each channel at s = 2 and s = 4 px

Channel	*Descriptor*	*A, s=2*	*B, s=2*	*C, s=2*	*D, s=2*	*A, s=4*	*B, s=4*	*C, s=4*	*D, s=4*
D1	Mean |∂θG|	0.091	0.101	0.025	0.047	0.053	0.107	0.006	0.045
D2	Energy (∂θG)²	0.186	0.182	0.041	0.087	0.107	0.198	0.015	0.077
D3	Kurtosis of ∂θG	0.017	0.056	0.036	0.018	0.040	0.031	0.056	0.041
D4	Entropy of ∂θG (bits)	0.001	0.002	0.002	0.001	0.001	0.001	0.001	0.001
D5	Mean |∂²θG|	0.130	0.127	0.043	0.064	0.100	0.123	0.018	0.064
D6	GLCM contrast	0.327	0.355	0.283	0.324	0.096	0.177	0.058	0.104
D7	GLCM homogeneity	0.059	0.074	0.048	0.061	0.021	0.042	0.013	0.024
D8	GLCM energy	0.145	0.176	0.131	0.152	0.043	0.090	0.025	0.054
D9	GLCM correlation	0.055	0.032	0.039	0.043	0.022	0.026	0.014	0.022
D10	Autocorrelation (lag 2s)	0.124	0.070	0.051	0.077	0.076	0.104	0.053	0.075

Interpretation. The modulation is small (< 0.2) for most channels, because the oriented structures are weak in these tissue panels. The exception is GLCM contrast D6 (modulation 0.28–0.35 at s = 2 px in all panels, including the near-isotropic panel C), which therefore mainly reflects the rounding of diagonal GLCM offsets to whole pixels and should not be interpreted as tissue anisotropy; the same caution applies to D8. Gradient channels (D2, D5) are modulated only in A and B (D2: 0.19 and 0.18) and are almost flat in C (0.041). Entropy D4 is practically independent of orientation (< 0.003).

Morphometric cross-check: unstained vacuole-like objects

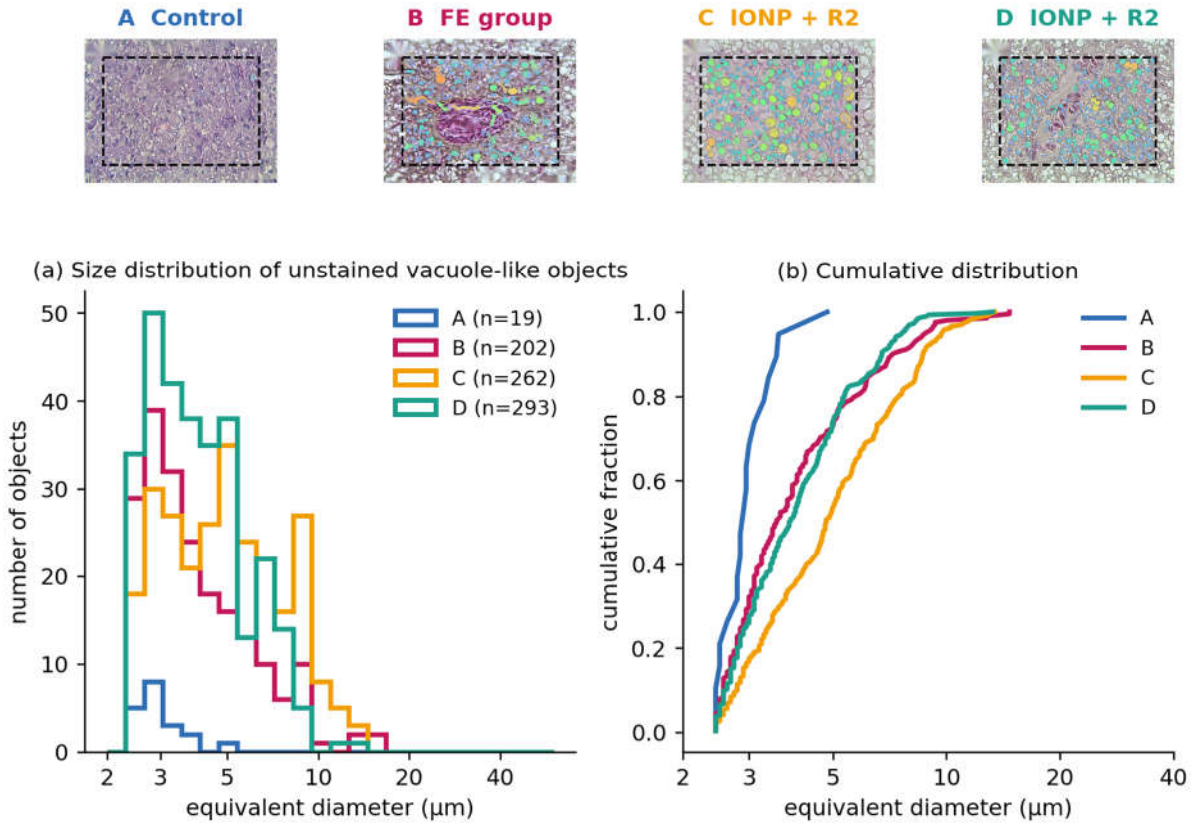


Figure 13. Segmentation of unstained vacuole-like objects (colour = equivalent diameter, 0–20 µm; dashed line: global ROI) and their size distributions.

Table 10

Vacuole-like object morphometry inside the global ROI (objects ≥ 20 px not touching the ROI border) and two tensor-derived quantities for comparison

Panel	*Unstained area (%)*	*Objects (n)*	*Median diameter (µm)*	*90th percentile (µm)*	*A (s = 2)*	*GLCM energy (s = 2)*
A	2.0	19	2.9	3.6	0.186	0.058
B	17.5	202	3.5	7.2	0.182	0.025
C	31.1	262	4.8	8.7	0.041	0.055
D	22.1	293	3.8	6.7	0.087	0.046

Interpretation. The unstained-area fraction increases from 2.0 % in the control to 17.5 % in B, 22.1 % in D and 31.1 % in C, in the same order as the visual impression and the source legend (macrosteatosis in C). The largest vacuoles are found in C (median 4.8 µm; 90th percentile 8.7 µm) and B (90th percentile 7.2 µm), and the smallest in A, where only 19 objects were detected, in agreement with the microsteatosis annotated in the control panel. This simple morphometric quantity separates the four panels much more clearly than the global texture channels D4, D7 and D9, whereas the anisotropy index and the multiscale gradient channels capture a different aspect of the images (orientation and scale distribution). The two kinds of measurement are therefore complementary. The caveat is that thresholds were fixed and merged vacuoles are counted as single objects, so diameters are approximate.

Regional analysis (R = 4)

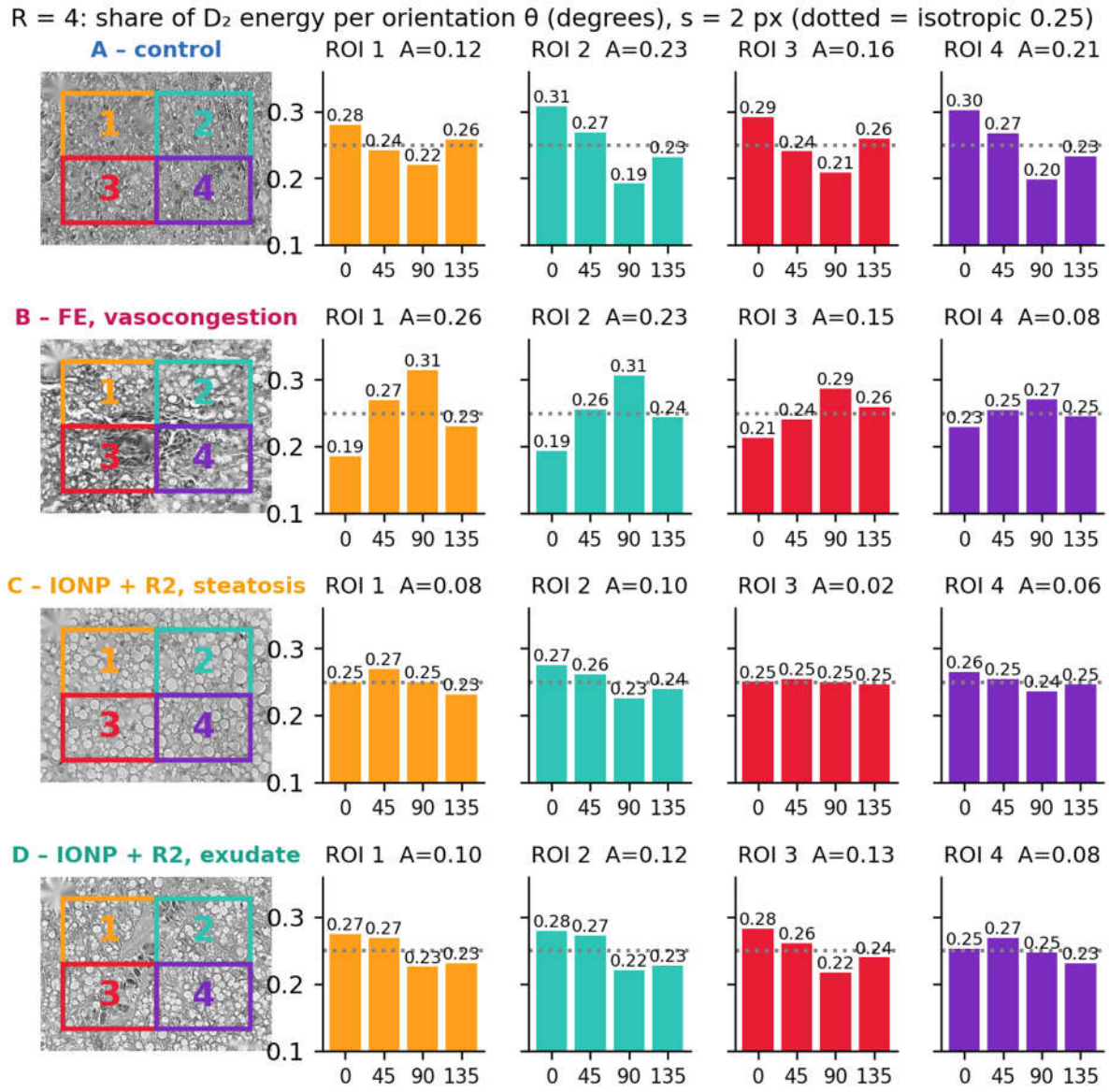


Figure 14. Four-region analysis: ROI layout (left) and share of D_2 energy per orientation at s = 2 px in each ROI, with the anisotropy index A of each ROI.

Table 11

D_2 energy share per orientation (s = 2 px), anisotropy index A and texture axis for the global ROI and the four regional ROIs

Panel	*ROI*	*θ = 0°*	*θ = 45°*	*θ = 90°*	*θ = 135°*	*A*	*Texture axis*
A	ROI = 1	0.297	0.255	0.203	0.245	0.186	93°
	ROI 1	0.280	0.242	0.220	0.258	0.118	82°
	ROI 2	0.308	0.268	0.192	0.232	0.232	99°
	ROI 3	0.291	0.240	0.209	0.260	0.164	83°
	ROI 4	0.302	0.267	0.198	0.233	0.209	99°
B	ROI = 1	0.204	0.255	0.296	0.245	0.182	177°
	ROI 1	0.185	0.269	0.315	0.231	0.259	172°
	ROI 2	0.194	0.256	0.306	0.244	0.226	177°
	ROI 3	0.213	0.241	0.287	0.259	0.149	7°
	ROI 4	0.229	0.254	0.271	0.246	0.083	174°
C	ROI = 1	0.260	0.260	0.240	0.240	0.041	112°
	ROI 1	0.250	0.269	0.250	0.231	0.075	135°
	ROI 2	0.275	0.261	0.225	0.239	0.099	102°
	ROI 3	0.250	0.254	0.250	0.246	0.017	134°
	ROI 4	0.264	0.254	0.236	0.246	0.057	98°

Panel	*ROI*	*θ = 0°*	*θ = 45°*	*θ = 90°*	*θ = 135°*	*A*	*Texture axis*
D	ROI = 1	0.272	0.268	0.228	0.232	0.087	110°
	ROI 1	0.274	0.269	0.226	0.231	0.097	109°
	ROI 2	0.280	0.272	0.220	0.228	0.119	108°
	ROI 3	0.283	0.260	0.217	0.240	0.130	99°
	ROI 4	0.253	0.269	0.247	0.231	0.076	130°

Table 12

Anisotropy index A and texture axis (A / axis) in each regional ROI at the four scales

Panel	*Scale*	*ROI 1*	*ROI 2*	*ROI 3*	*ROI 4*
A	s = 1	0.10 / 86°	0.26 / 95°	0.15 / 82°	0.22 / 97°
	s = 2	0.12 / 82°	0.23 / 99°	0.16 / 83°	0.21 / 99°
	s = 4	0.09 / 75°	0.13 / 103°	0.07 / 81°	0.14 / 106°
	s = 8	0.11 / 49°	0.05 / 65°	0.04 / 67°	0.04 / 70°
B	s = 1	0.22 / 171°	0.22 / 177°	0.15 / 7°	0.10 / 179°
	s = 2	0.26 / 172°	0.23 / 177°	0.15 / 7°	0.08 / 174°
	s = 4	0.28 / 171°	0.22 / 176°	0.22 / 5°	0.05 / 167°
	s = 8	0.25 / 6°	0.21 / 172°	0.31 / 179°	0.14 / 3°
C	s = 1	0.07 / 122°	0.14 / 97°	0.02 / 112°	0.10 / 101°
	s = 2	0.08 / 135°	0.10 / 102°	0.02 / 134°	0.06 / 98°
	s = 4	0.08 / 150°	0.04 / 90°	0.02 / 22°	0.00 / 164°
	s = 8	0.14 / 5°	0.06 / 98°	0.17 / 1°	0.10 / 139°
D	s = 1	0.11 / 111°	0.11 / 113°	0.13 / 102°	0.10 / 126°
	s = 2	0.10 / 109°	0.12 / 108°	0.13 / 99°	0.08 / 130°
	s = 4	0.11 / 105°	0.13 / 107°	0.08 / 94°	0.10 / 134°
	s = 8	0.11 / 63°	0.05 / 119°	0.22 / 45°	0.10 / 151°

Interpretation. In the control panel A, all four ROIs have a similar vertical axis (82°, 99°, 83°, 99°) with A between 0.12 and 0.23, so the directional organization is spatially coherent. In panel B the axis is horizontal in all ROIs (172°, 177°, 7°, 174°), but A decreases from 0.26 in ROI 1 to 0.08 in ROI 4: the anisotropy is concentrated in the regions crossed by the vessel and its boundaries, while the lower-right region is nearly isotropic. This regional gradient is hidden by the single global value (A = 0.18). Panels C and D are weakly anisotropic in all ROIs (A ≤ 0.10 and ≤ 0.13 respectively), and their axes are scattered, as expected for near-isotropic fields. At s = 8 px the regional values of A and the axes become unstable in all panels (Table 12), in line with the small effective sample of structures at this scale.

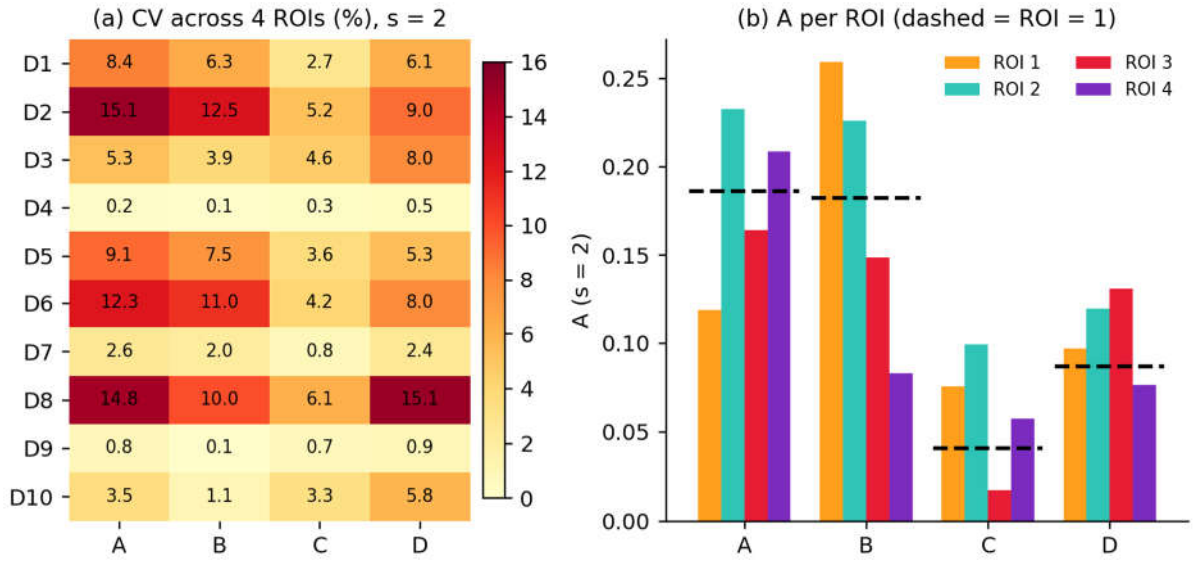


Figure 15. Spatial heterogeneity. (a) Coefficient of variation (%) of each channel across the four ROIs (s = 2 px, mean over θ). (b) Anisotropy index A in each ROI; dashed lines: global value (R = 1).

Table 13

Coefficient of variation (%) of each channel (s = 2 px, mean over θ) across the four ROIs, and the internal consistency check between R = 1 and R = 4

Channel	*Descriptor*	*A*	*B*	*C*	*D*
D1	Mean |∂θG|	8.4	6.3	2.7	6.1
D2	Energy $(\partial\theta G)^2$	15.1	12.5	5.2	9.0
D3	Kurtosis of ∂θG	5.3	3.9	4.6	8.0
D4	Entropy of ∂θG (bits)	0.2	0.1	0.3	0.5
D5	Mean $\|\partial^2\theta G\|$	9.1	7.5	3.6	5.3
D6	GLCM contrast	12.3	11.0	4.2	8.0
D7	GLCM homogeneity	2.6	2.0	0.8	2.4
D8	GLCM energy	14.8	10.0	6.1	15.1
D9	GLCM correlation	0.8	0.1	0.7	0.9
D10	Autocorrelation (lag 2s)	3.5	1.1	3.3	5.8
Check	mean of ROI D_2 − global D_2 (relative)	2e-16	0e+00	0e+00	2e-16

Interpretation. The descriptors differ strongly in regional stability. Entropy (D4), GLCM correlation (D9), homogeneity (D7) and autocorrelation (D10) vary by at most 5.8 % between regions in every panel, whereas GLCM energy (D8), gradient energy (D2) and GLCM contrast (D6) vary by up to 15.1 %, 15.1 % and 12.3 %. The most homogeneous panel is C (D2 CV 5.2 %), consistent with a uniform distribution of vacuoles, while the control A has the highest variability in D2 (15.1 %) and a high variability in D8 (14.8 %). The consistency check confirms that the regional means reproduce the global values for the mean-based channels (relative difference below 10^{-12}, i.e. numerical noise), as must be the case for an arithmetic mean over equal areas.

Redundancy among descriptors and similarity of the panels

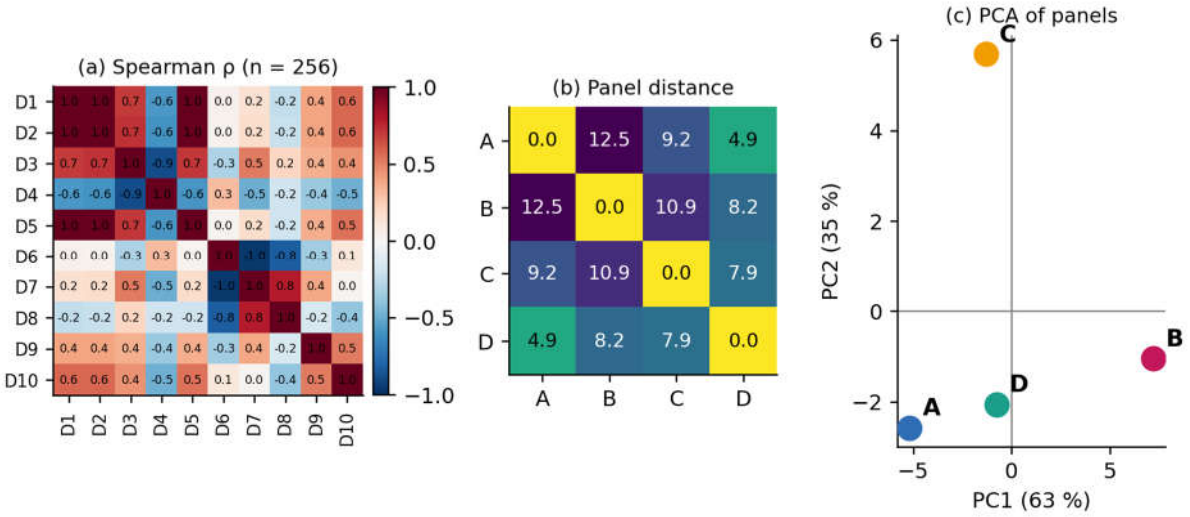


Figure 16. (a) Spearman correlation between channels over all R = 4 tensor entries (n = 256). (b) Euclidean distance between panels in the standardized feature space (eight channels × four scales). (c) Principal component analysis of the same features

Table 14

Channel pairs with Spearman |ρ| ≥ 0.8 (n = 256 tensor entries of the R = 4 configuration, four panels)

Pair	*Spearman ρ*	*Remark*
D1 – D2	1.00	redundant (|ρ| ≥ 0.95)
D1 – D5	0.99	redundant (|ρ| ≥ 0.95)
D2 – D5	0.99	redundant (|ρ| ≥ 0.95)
D6 – D7	−0.96	redundant (|ρ| ≥ 0.95)
D3 – D4	−0.89	strongly associated
D6 – D8	−0.83	strongly associated

Table 15

Distance between panels in the standardized feature space and principal-component scores (PC1 63 %, PC2 35 % of the variance)

Panel	*A*	*B*	*C*	*D*	*PC1*	*PC2*
A	0.0	12.5	9.2	4.9	−5.18	−2.58
B	12.5	0.0	10.9	8.2	7.21	−1.05
C	9.2	10.9	0.0	7.9	−1.28	5.69
D	4.9	8.2	7.9	0.0	−0.75	−2.06

Interpretation. D1, D2 and D5 are practically equivalent (ρ = 1.00, 0.99 and 0.99): all measure gradient amplitude at the same scale, and one of them can represent the group. GLCM contrast and homogeneity are almost perfectly anti-correlated (ρ = −0.96), and kurtosis and entropy are strongly anti-correlated (ρ = −0.89). Channels D9 and D10 show only moderate associations with the others, providing complementary information. In the exploratory feature space the closest pair of panels is A–D (distance 4.9) and the most distant is A–B (12.5); PC1 (63 % of the variance) separates B from A and D, and PC2 (35 %) separates C. With four panels these coordinates are descriptive only and should not be read as a classification.

Sensitivity to ROI size

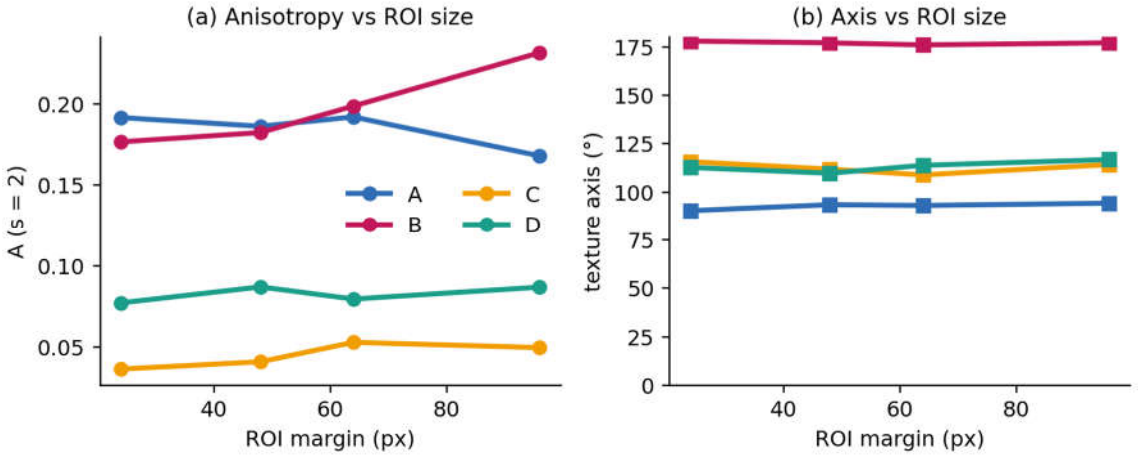


Figure 17. Sensitivity of the anisotropy index A (s = 2 px) and of the texture axis to the ROI margin (a larger margin means a smaller central ROI).

Table 16

Sensitivity of the anisotropy index and the axis to the size of the global ROI

Panel	*Margin (px)*	*ROI (px)*	*A, s = 2*	*A, s = 4*	*Axis, s = 2*
A	24	462 × 334	0.191	0.126	90°
	48	414 × 286	0.186	0.107	93°
	64	382 × 254	0.192	0.107	93°
	96	318 × 190	0.168	0.081	94°
B	24	462 × 334	0.176	0.192	178°
	48	414 × 286	0.182	0.198	177°
	64	382 × 254	0.198	0.214	176°
	96	318 × 190	0.231	0.281	177°
C	24	462 × 334	0.037	0.031	116°
	48	414 × 286	0.041	0.015	112°
	64	382 × 254	0.053	0.021	109°
	96	318 × 190	0.050	0.022	114°
D	24	462 × 334	0.077	0.074	113°
	48	414 × 286	0.087	0.077	110°
	64	382 × 254	0.079	0.082	114°
	96	318 × 190	0.087	0.081	117°

Interpretation. At s = 2 px, the anisotropy index of panels A, C and D changed little over the tested range of ROI sizes (by at most 0.024 in absolute value), and their axes changed by at most 7°. At s = 4 px the sensitivity was larger: A of panel A

decreased from 0.126 to 0.081 (−36 %) as the margin increased from 24 to 96 px, and A of panel C, which is close to the isotropy floor, varied between 0.015 and 0.031. Panel B is the most sensitive: A rises from 0.18 to 0.23 at s = 2 px (from 0.19 to 0.28 at s = 4 px) as the ROI shrinks towards the central vessel, while its axis stays horizontal (176–178°). This is consistent with a dominant contribution of the vessel to the anisotropy of B, although shrinking the ROI also changes the proportions of parenchyma and boundaries that it contains. The choice of a 48-pixel margin is therefore a reasonable compromise between tissue coverage and exclusion of border effects.

Agreement of the measurements with the theoretical relations. The relations of Section 2.8 were checked on the tensors of Supplementary Table S1 (Table 17). The four D_2 entries of every global and regional tensor satisfied the constraint $D_2(0) + D_2(\pi/2) = D_2(\pi/4) + D_2(3\pi/4)$ to within 6×10^{-6} of the trace when evaluated on the unrounded values (the three-significant-digit values of Tables A1–A4 satisfy it only to within their rounding, at most 0.3 % of the trace), confirming that the D_2 block is the quadratic form of a 2 × 2 structure matrix. The index computed from the structure matrix, A, was equal to or larger than the sampled index A_4 in all panels and scales and within the bounds of Eq. (5); the difference was negligible where the texture axis lies close to a sampled orientation (panel A, axis 93°; panel B, axis 177°) and largest where it lies between two orientations (panel D, axis 110°: A_4 = 0.087 versus A = 0.112 at s = 2 px). The pooling inequality of Eq. (7) held in all 16 combinations of panel and scale.

Table 17

Sampled anisotropy index A_4 (as in Table 6), anisotropy index from the structure matrix A (Eq. (4)) and energy-weighted mean of the four regional values (right-hand side of Eq. (7)), at s = 2 and s = 4 px

Panel	*A_4, s = 2*	*A, s = 2*	*$\Sigma E_r A_r / \Sigma E_r$, s = 2*	*A_4, s = 4*	*A, s = 4*	*$\Sigma E_r A_r / \Sigma E_r$, s = 4*
A – control	0.186	0.187	0.194	0.107	0.110	0.121
B – FE group	0.182	0.183	0.187	0.198	0.200	0.204
C – IONP + R2 (steatosis)	0.041	0.056	0.067	0.015	0.017	0.041
D – IONP + R2 (exudate)	0.087	0.112	0.120	0.077	0.101	0.114

Interpretation. The gap between the global index and the energy-weighted regional mean is small in panels A and B (0.004–0.011), whose regional axes agree (Table 11), and largest in panel C at s = 4 px (0.017 versus 0.041), whose regional axes are scattered: the global value of C is low partly because weakly oriented regions with different axes cancel each other, which is the mechanism expressed by Eq. (7). Within each region, the low anisotropy of the vacuolated panels is consistent with the dilution relation of Eq. (6): the vacuole-like objects, whose area fraction is 31 % in C and 22 % in D (Table 10), have round boundaries that add gradient energy in all directions. These checks confirm that the reported indices obey the relations expected from their definition; they do not by themselves establish a biological interpretation.

General discussion. The analysis shows that, within the four selected panels, the ten-channel tensor describes several aspects of the visual differences between control, congested and steatotic liver, while other aspects remain invisible to the global descriptors. Directional organization was measurable in the control panel (A = 0.19 at s = 2 px) and the vasocongested panel (A = 0.18), but was weak or absent in the two vacuolated panels. The control texture is dominated by fine, partly oriented structure, panel B by a large oriented structure (the vessel), which appears to dominate the coarse scales and the regions it crosses, and panels C and D by rounded vacuoles that generate gradient energy at all orientations. The tensor representation made these differences explicit as separate dimensions (scale, orientation and region), which is the purpose of the hierarchical framework. The theoretical relations of Section 2.8 account for two of these observations: round vacuole boundaries add nearly isotropic gradient energy and therefore dilute the anisotropy index (Eq. (6)), and summarizing a panel whose regions

have different axes can only lower the global index (Eq. (7)), as observed for panel C (Table 17).

Two methodological findings deserve emphasis. First, regional analysis was informative: the single global anisotropy of panel B (A = 0.18) conceals a gradient between regions (A = 0.26 to 0.08), and the stability of the descriptors across regions differs by channel, with entropy, correlation, homogeneity and autocorrelation being stable and energy-type channels being spatially variable. This supports the use of regional measurements alongside global summaries, as stated in the Introduction, while noting that the regional values describe variability inside one image and not between animals. Second, global texture descriptors can be insensitive to changes that are obvious to the eye. The steatotic panel C (31 % unstained area) is nearly indistinguishable from the control in several channels at s = 2 px (D4, D7, D8, D9), and the entropy varies only between 3.92 and 4.05 bits over all panels, scales and orientations, close to the value of about 4.05 bits expected for a Gaussian distribution with the 32-bin discretization. A direct morphometric quantity (unstained area and vacuole size) separated the panels more clearly. Texture descriptors should therefore be interpreted as descriptions of image organization, complementary to, and not substitutes for, histopathological scoring such as the protocols used in fish histology (Bernet et al., 1999).

The relationship between the descriptors and the lesions reported by Martins et al. (2022) should be interpreted cautiously. The source legend identifies vasocongestion in B, macrosteatosis in C and exudate with red blood cells in D, and the present results are compatible with these descriptions: panel B contains a large, strongly stained structure that dominates the coarse-scale energy and the long-range correlation, panel C has the largest vacuolar fraction and an almost isotropic gradient field, and panel D has an intermediate vacuolar fraction with a weak oriented component along the vessel containing the exudate. However, the analysis does not show that any descriptor measures a specific lesion, and differences between panels may also reflect staining, illumination and compression differences that the z-score normalization cannot remove, particularly for non-linear descriptors such as kurtosis and the GLCM features.

The practical lessons for applying the framework to histological images are as follows: (i) the pixel calibration should be verified, because the scales s = 1–8 px correspond here to only 0.5–3.9 µm, i.e. well below the size of a vacuole or a hepatocyte, so that fine scales primarily probe membranes and edges; (ii) larger scales or a larger scale set (for example s up to 16–32 px) would be needed to probe the cellular scale at this resolution; (iii) the redundant gradient channels (D1, D2, D5) can be collapsed; (iv) the diagonal orientations of GLCM-based channels should be treated with caution because of offset rounding; and (v) the ROI size should be reported, because the anisotropy of panel B depends on whether the vessel is within the ROI.

Limitations. Only one panel per condition was analysed, extracted from a published figure; the panels are not independent biological replicates and no statistical inference was attempted. Regions of interest within a panel are subsamples of the same tissue section. The panels are JPEG-compressed figure panels without original microscope files; the effective resolution is lower than the pixel grid suggests, and compression noise contributes to the gradient energy at the finest scales. The panels were originally annotated with arrows, stars and labels; the annotations were removed by inpainting (1.2–2.0 % of the ROI pixels), which slightly alters the local texture at those positions. Illumination and staining differ between panels (e.g. panel D is greener and panels C and D are paler). The z-score normalization removes linear differences but not the effects on non-linear descriptors. The orientation analysis uses four directions, so the axis estimate has limited angular resolution; the anisotropy values below about 0.05 are close to the isotropy floor, and the GLCM-based channels are affected by integer rounding of diagonal offsets. The vacuole segmentation used fixed thresholds and merges touching objects; diameters are approximate and are intended only as a cross-check of the tensor results. The biological descriptions are taken from the source legend and were not verified independently.

Conclusions. A multiscale and multidirectional descriptor tensor (10 × 4 × 4 × R) was computed for four published guppy liver histology panels using a global ROI (160 entries per panel) and a four-region partition (640 entries per panel). The tensor provided a structured quantitative description of image texture, documented in sufficient detail to be recomputed from the published panels, in which scale, orientation and region are separate dimensions. In the analysed panels, the control and the vasocongested panels showed measurable directional organization (vertical and horizontal texture axes, respectively), whereas the steatotic panels were nearly isotropic; the vasocongested panel had the broadest scale distribution of gradient energy; regional analysis revealed spatial variability that the global values concealed; and entropy, correlation, homogeneity and autocorrelation were spatially stable while energy-type channels were not. Several descriptors were redundant (D1, D2, D5), and global texture descriptors alone did not separate the control from the steatotic panel at the finest scales, in contrast to a simple vacuole morphometry. These findings are exploratory and image-specific. Biological generalization or diagnostic use would require independent replicates, standardized image acquisition with original microscope files, and validation against independent histopathological assessment.

Data Availability. The analysis code, ROI coordinates and unrounded numerical results are available from the corresponding author upon request. The complete descriptor tensors (160 + 640 entries per panel) are provided as Supplementary Table S1.

Copyright and Permissions. Figure 2a reproduces panels A–D of Figure 2 of Martins et al. (2022), Environmental Toxicology, 37(9), 2244–2258, © 2022 Wiley Periodicals LLC; Figures 1–5, 7, 9, 13 and 14 contain renderings derived from these panels. Reproduced and adapted with permission from John Wiley and Sons (Licence Number 6380941362622). All quantitative results, tables and the remaining figure elements were produced by the author.

Relationship to Other Work. The descriptor tensor and its reference implementation were introduced and verified by Ţălu (2027a) and applied to guppy muscle by Ţălu (2026); the present paper applies the same definitions to new material and does not reproduce their figures or results.

Funding. This research received no external funding.

Conflict of Interest. The author declares no conflict of interest.

References

Bernet, D., Schmidt, H., Meier, W., Burkhardt-Holm, P., & Wahli, T. (1999). Histopathology in fish: Proposal for a protocol to assess aquatic pollution. *Journal of Fish Diseases, 22*(1), 25–34. https://doi.org/10.1046/j.1365-2761.1999.00134.x

Bigün, J., & Granlund, G. H. (1987). Optimal orientation detection of linear symmetry. In *Proceedings of the First International Conference on Computer Vision* (pp. 433–438). London.

Bradski, G. (2000). The OpenCV library. *Dr. Dobb's Journal of Software Tools, 25*(11), 120-125.

Depeursinge, A. (2017). Multiscale and multidirectional biomedical texture analysis: Finding the needle in the haystack. In A. Depeursinge, O. S. Al-Kadi, & J. R. Mitchell (Eds.), *Biomedical texture analysis* (pp. 29–53). Academic Press. https://doi.org/10.1016/B978-0-12-812133-7.00002-8

Freeman, W. T., & Adelson, E. H. (1991). The design and use of steerable filters. *IEEE Transactions on Pattern Analysis and Machine Intelligence, 13*(9), 891–906. https://doi.org/10.1109/34.93808

Goshisht, M. K., Goshisht, A., Bajpai, A., & Bajpai, A. (2025). Recent advances in biomedical applications of smart nanomaterials: A comprehensive review. *RSC Pharmaceutics, 2*, 1227. https://doi.org/10.1039/d5pm00137d

Gurcan, M. N., Boucheron, L. E., Can, A., Madabhushi, A., Rajpoot, N. M., & Yener, B. (2009). Histopathological image analysis: A review. *IEEE Reviews in Biomedical Engineering, 2*, 147–171. https://doi.org/10.1109/RBME.2009.2034865

Haralick, R. M., Shanmugam, K., & Dinstein, I. (1973). Textural features for image classification. *IEEE Transactions on Systems, Man, and Cybernetics, SMC-3*(6), 610–621. https://doi.org/10.1109/TSMC.1973.4309314

Harris, C. R., Millman, K. J., van der Walt, S. J., et al. (2020). Array programming with NumPy. *Nature, 585*, 357–362. https://doi.org/10.1038/s41586-020-2649-2

Hunter, J. D. (2007). Matplotlib: A 2D graphics environment. *Computing in Science & Engineering, 9*(3), 90–95. https://doi.org/10.1109/MCSE.2007.55

Jagadeesh, P., Rangappa, S. M., & Siengchin, S. (2024). Advanced characterization techniques for nanostructured materials in biomedical applications. *Advanced Industrial and Engineering Polymer Research, 7*(1), 122–143. https://doi.org/10.1016/j.aiepr.2023.03.002

Lima-Faria, J. M., Guimarães, L. N., Silva, V. C., Lima, E. C. O., & Sabóia-Morais, S. M. T. (2021). Recovery trend to co-exposure of iron oxide nanoparticles (γ-Fe_2O_3) and glyphosate in liver tissue of the fish *Poecilia reticulata*. *Chemosphere, 282*, 130993. https://doi.org/10.1016/j.chemosphere.2021.130993

Lindeberg, T. (1994). Scale-space theory: A basic tool for analysing structures at different scales. *Journal of Applied Statistics, 21*(1–2), 225–270. https://doi.org/10.1080/757582976

Lindeberg, T. (1998). Feature detection with automatic scale selection. *International Journal of Computer Vision, 30*(2), 79–116. https://doi.org/10.1023/A:1008045108935

Macenko, M., Niethammer, M., Marron, J. S., et al. (2009). A method for normalizing histology slides for quantitative analysis. In *Proceedings of the IEEE International Symposium on Biomedical Imaging (ISBI)* (pp. 1107–1110). https://doi.org/10.1109/ISBI.2009.5193250

Mardia, K. V., & Jupp, P. E. (2000). *Directional statistics*. John Wiley & Sons. https://doi.org/10.1002/9780470316979

Martins, L. K. L., Lima-Faria, J. M., Guimarães, L. N., Silva, V. C., Moreira, P. C., & Sabóia-Morais, S. M. T. (2022). Co-exposure of iron oxide nanoparticles and glyphosate-based herbicide promote liver toxicity in guppy (*Poecilia reticulata*): A histochemical and ultrastructural approach. *Environmental Toxicology, 37*(9), 2244–2258. https://doi.org/10.1002/tox.23591

Qualhato, G., Sabóia-Morais, S. M. T., Silva, L. D., & Rocha, T. L. (2018). Melanomacrophage response and hepatic histopathologic biomarkers in the guppy *Poecilia reticulata* exposed to iron oxide (maghemite) nanoparticles. *Aquatic Toxicology, 198*, 63–72. https://doi.org/10.1016/j.aquatox.2018.02.014

Roszkowski, S., & Durczynska, Z. (2025). Advantages and limitations of nanostructures for biomedical applications. *Advances in Clinical and Experimental Medicine, 34*(3), 447–456. https://doi.org/10.17219/acem/186846

Ruifrok, A. C., & Johnston, D. A. (2001). Quantification of histochemical staining by color deconvolution. *Analytical and Quantitative Cytology and Histology, 23*(4), 291–299.

Santos, A. P. R., Rocha, T. L., Borges, C. L., Bailão, A. M., de Almeida Soares, C. M., & de Sabóia-Morais, S. M. T. (2017). A glyphosate-based herbicide induces histomorphological and protein expression changes in the liver of the female guppy *Poecilia reticulata*. *Chemosphere, 168*, 933–943. https://doi.org/10.1016/j.chemosphere.2016.10.116

Spearman, C. (1904). The proof and measurement of association between two things. *The American Journal of Psychology, 15*(1), 72–101. https://doi.org/10.2307/1412159

Telea, A. (2004). An image inpainting technique based on the fast-marching method. *Journal of Graphics Tools, 9*(1), 23–34. https://doi.org/10.1080/10867651.2004.10487596

Ţălu, Ş. (2026). Application of the hierarchical texture-descriptor tensor to histological muscle sections of *Poecilia reticulata*. *Poeciliid Research, 16*(1), 62-74. https://doi.org/10.67784/0096

Ţălu, Ş. (2027a). A hierarchical tensor framework for quantitative multiscale and multidirectional biomedical texture characterization. *Human & Veterinary Medicine, 19*(1), 32-53. https://doi.org/10.67784/0095

Ţălu, Ş. (2027b). Coherence, alignment and fibre-profile geometry in a hierarchical texture-descriptor tensor: Application to H&E sections of skeletal muscle in wild boar (*Sus scrofa*) and domestic pigs. *Porcine Research, 17*(1), 1-22. https://doi.org/10.67784/0098

Ţălu, Ş. (2027c). Descriptor-tensor texture analysis of myostatin-edited rabbit muscle: A two-study replication. *Rabbit Genetics, 17*(1), 10-24. https://doi.org/10.67784/0097

Ţălu, Ş. (2027d). Scale and orientation signatures of soil structure in thin sections: A hierarchical descriptor tensor applied to greenhouse soils under conventional, pollution-free and organic management. *Advances in Environmental Sciences, 19*(1), 53-70. https://doi.org/10.67784/0099

van der Walt, S., Schönberger, J. L., Nunez-Iglesias, J., Boulogne, F., Warner, J. D., Yager, N., Gouillart, E., Yu, T., & the scikit-image contributors. (2014). scikit-image: Image processing in Python. *PeerJ, 2*, e453. https://doi.org/10.7717/peerj.453

Virtanen, P., Gommers, R., Oliphant, T. E., et al. (2020). SciPy 1.0: Fundamental algorithms for scientific computing in Python. *Nature Methods, 17*, 261–272. https://doi.org/10.1038/s41592-019-0686-2

Wolf, J. C., & Wolfe, M. J. (2005). A brief overview of nonneoplastic hepatic toxicity in fish. *Toxicologic Pathology, 33*(1), 75–85. https://doi.org/10.1080/01926230590890187

Zuiderveld, K. (1994). Contrast limited adaptive histogram equalization. In P. S. Heckbert (Ed.), *Graphics gems IV* (pp. 474–485). Academic Press.

Zwanenburg, A., Vallières, M., Abdalah, M. A., et al. (2020). The Image Biomarker Standardization Initiative: Standardized quantitative radiomics for high-throughput image-based phenotyping. *Radiology, 295*(2), 328–338. https://doi.org/10.1148/radiol.2020191145

Appendix A. Complete tensors for R = 1

Tables A1–A4 give all 160 entries of the global tensor of each panel (10 channels × 4 scales × 4 orientations). The regional tensors (640 entries per panel) are provided in Supplementary Table S1.

Table A1

Global tensor (R = 1) of panel A – control.

Channel	Scale	θ = 0°	θ = 45°	θ = 90°	θ = 135°
D1	s = 1	0.28	0.26	0.233	0.256
	s = 2	0.108	0.101	0.0902	0.0988
	s = 4	0.035	0.034	0.0315	0.033
	s = 8	0.0104	0.00993	0.01	0.0104
D2	s = 1	0.139	0.118	0.0945	0.115
	s = 2	0.0207	0.0178	0.0142	0.017
	s = 4	0.00207	0.00192	0.00167	0.00182
	s = 8	0.000174	0.000158	0.000162	0.000177
D3	s = 1	4.28	4.07	4.05	4.21
	s = 2	4.19	4.06	4.09	4.14
	s = 4	3.85	3.7	3.56	3.73
	s = 8	3.24	3.32	3.32	3.47

Channel	Scale	θ = 0°	θ = 45°	θ = 90°	θ = 135°
D4	s = 1	4	4.01	4.02	4.01
	s = 2	4.01	4.01	4.02	4.01
	s = 4	4.03	4.03	4.03	4.03
	s = 8	4.04	4.04	4.04	4.04
D5	s = 1	0.257	0.237	0.205	0.232
	s = 2	0.0607	0.0544	0.0467	0.0531
	s = 4	0.0103	0.00961	0.00847	0.00918
	s = 8	0.00146	0.00142	0.00139	0.00144
D6	s = 1	1.21	1.84	0.883	1.79
	s = 2	1.28	0.673	0.945	0.65
	s = 4	1.08	1.11	0.917	1.07
	s = 8	0.9	0.907	0.858	1.01
D7	s = 1	0.68	0.625	0.716	0.629
	s = 2	0.672	0.753	0.708	0.756
	s = 4	0.684	0.676	0.705	0.683
	s = 8	0.696	0.694	0.705	0.685
D8	s = 1	0.0437	0.036	0.0492	0.0366
	s = 2	0.0484	0.064	0.0546	0.0647
	s = 4	0.0557	0.0544	0.0594	0.0554
	s = 8	0.06	0.0595	0.0609	0.0572
D9	s = 1	0.848	0.769	0.89	0.776
	s = 2	0.808	0.899	0.859	0.903
	s = 4	0.801	0.795	0.831	0.803
	s = 8	0.822	0.82	0.83	0.8
D10	s = 1	0.563	0.786	0.694	0.792
	s = 2	0.484	0.503	0.622	0.524
	s = 4	0.492	0.481	0.56	0.494
	s = 8	0.552	0.608	0.572	0.549

Table A2

Global tensor (R = 1) of panel B – FE group.

Channel	Scale	θ = 0°	θ = 45°	θ = 90°	θ = 135°
D1	s = 1	0.2	0.224	0.242	0.221
	s = 2	0.105	0.119	0.129	0.117
	s = 4	0.0453	0.0516	0.0561	0.0503
	s = 8	0.015	0.0175	0.0195	0.0176
D2	s = 1	0.0746	0.0913	0.105	0.0886
	s = 2	0.0196	0.0244	0.0283	0.0235
	s = 4	0.00342	0.00438	0.0051	0.00414
	s = 8	0.000372	0.000482	0.000593	0.000483
D3	s = 1	4.46	4.18	4.03	4.09
	s = 2	4	3.8	3.57	3.66
	s = 4	3.58	3.54	3.37	3.37
	s = 8	3.48	3.01	3.01	2.93
D4	s = 1	3.99	4	4.01	4
	s = 2	4.02	4.03	4.03	4.03
	s = 4	4.04	4.04	4.04	4.04
	s = 8	4.04	4.05	4.04	4.04
D5	s = 1	0.15	0.174	0.19	0.17
	s = 2	0.0469	0.0537	0.0605	0.053
	s = 4	0.0115	0.0132	0.0148	0.0129
	s = 8	0.00206	0.00243	0.00283	0.00239
D6	s = 1	1.17	2.5	1.57	2.44
	s = 2	1.45	0.993	2.01	0.958
	s = 4	1.49	2.06	2.14	1.96
	s = 8	1.27	1.75	1.91	1.77
D7	s = 1	0.694	0.599	0.653	0.602
	s = 2	0.656	0.699	0.607	0.704
	s = 4	0.638	0.594	0.586	0.6
	s = 8	0.657	0.603	0.591	0.601
D8	s = 1	0.0235	0.0164	0.0201	0.0166
	s = 2	0.0233	0.0275	0.0195	0.0279
	s = 4	0.0255	0.0219	0.0213	0.0223
	s = 8	0.0287	0.0245	0.0236	0.0241
D9	s = 1	0.947	0.885	0.928	0.888
	s = 2	0.918	0.944	0.887	0.946
	s = 4	0.896	0.857	0.851	0.864
	s = 8	0.909	0.875	0.863	0.873
D10	s = 1	0.837	0.892	0.774	0.895
	s = 2	0.755	0.669	0.656	0.681

Channel	Scale	θ = 0°	θ = 45°	θ = 90°	θ = 135°
	s = 4	0.703	0.592	0.57	0.612
	s = 8	0.757	0.707	0.641	0.696

Table A3

Global tensor (R = 1) of panel C – IONP + R2 (steatosis)

Channel	Scale	θ = 0°	θ = 45°	θ = 90°	θ = 135°
D1	s = 1	0.245	0.241	0.226	0.231
	s = 2	0.111	0.11	0.105	0.106
	s = 4	0.0423	0.0424	0.0419	0.0421
	s = 8	0.0119	0.0124	0.0126	0.0122
D2	s = 1	0.121	0.117	0.104	0.108
	s = 2	0.0224	0.0224	0.0206	0.0207
	s = 4	0.00288	0.00294	0.00292	0.00285
	s = 8	0.000223	0.000242	0.000249	0.000231
D3	s = 1	5.23	5.26	5.37	5.33
	s = 2	4.11	4.28	4.41	4.21
	s = 4	3.08	3.23	3.45	3.13
	s = 8	2.99	2.89	2.86	3.03
D4	s = 1	3.92	3.92	3.92	3.92
	s = 2	3.99	3.99	3.98	3.99
	s = 4	4.04	4.04	4.03	4.05
	s = 8	4.05	4.05	4.05	4.04
D5	s = 1	0.21	0.206	0.186	0.195
	s = 2	0.0566	0.0566	0.0519	0.0529
	s = 4	0.0119	0.0119	0.0115	0.0115
	s = 8	0.00181	0.00188	0.00193	0.00185
D6	s = 1	0.769	1.28	0.682	1.19
	s = 2	1.02	0.606	0.96	0.572
	s = 4	1.47	1.65	1.49	1.6
	s = 8	1.56	1.84	1.72	1.76
D7	s = 1	0.757	0.699	0.771	0.706
	s = 2	0.707	0.771	0.717	0.778
	s = 4	0.634	0.622	0.639	0.623
	s = 8	0.619	0.6	0.608	0.601
D8	s = 1	0.058	0.0471	0.061	0.0482
	s = 2	0.0482	0.061	0.05	0.0626
	s = 4	0.0349	0.0333	0.035	0.0335
	s = 8	0.0297	0.0276	0.0282	0.0279
D9	s = 1	0.883	0.805	0.896	0.819
	s = 2	0.846	0.909	0.855	0.914
	s = 4	0.817	0.794	0.813	0.799
	s = 8	0.84	0.812	0.825	0.82
D10	s = 1	0.679	0.825	0.718	0.839
	s = 2	0.578	0.543	0.601	0.569
	s = 4	0.494	0.444	0.482	0.453
	s = 8	0.576	0.562	0.539	0.583

Table A4

Global tensor (R = 1) of panel D – IONP + R2 (exudate).

Channel	Scale	θ = 0°	θ = 45°	θ = 90°	θ = 135°
D1	s = 1	0.263	0.262	0.238	0.237
	s = 2	0.11	0.109	0.101	0.101
	s = 4	0.0396	0.0394	0.0362	0.0366
	s = 8	0.0122	0.0117	0.0118	0.0122
D2	s = 1	0.123	0.123	0.102	0.102
	s = 2	0.0215	0.0211	0.018	0.0184
	s = 4	0.00262	0.0026	0.00225	0.00227
	s = 8	0.000235	0.000222	0.00023	0.000243
D3	s = 1	3.85	3.9	4.02	4.14
	s = 2	3.82	3.81	3.95	3.92
	s = 4	3.37	3.3	3.58	3.51
	s = 8	2.9	3.21	3.57	3.24
D4	s = 1	4.01	4.01	4.01	4
	s = 2	4.02	4.02	4.01	4.01
	s = 4	4.04	4.04	4.03	4.03
	s = 8	4.04	4.04	4.03	4.04
D5	s = 1	0.232	0.236	0.203	0.206
	s = 2	0.0587	0.058	0.0516	0.0525
	s = 4	0.0112	0.0111	0.00986	0.0101
	s = 8	0.00176	0.00171	0.00162	0.00164

Channel	Scale	θ = 0°	θ = 45°	θ = 90°	θ = 135°
D6	s = 1	1.39	2.45	1.19	2.09
	s = 2	1.39	0.792	1.2	0.711
	s = 4	1.32	1.43	1.16	1.28
	s = 8	1.27	1.31	1.25	1.45
D7	s = 1	0.665	0.598	0.687	0.62
	s = 2	0.662	0.732	0.683	0.748
	s = 4	0.656	0.646	0.678	0.664
	s = 8	0.647	0.651	0.663	0.64
D8	s = 1	0.0299	0.0234	0.0324	0.0253
	s = 2	0.0385	0.0495	0.0417	0.0524
	s = 4	0.0446	0.0433	0.0483	0.0458
	s = 8	0.0398	0.04	0.0421	0.0386
D9	s = 1	0.884	0.795	0.901	0.825
	s = 2	0.845	0.912	0.866	0.921
	s = 4	0.825	0.809	0.845	0.829
	s = 8	0.85	0.844	0.851	0.828
D10	s = 1	0.655	0.806	0.707	0.837
	s = 2	0.565	0.536	0.625	0.588
	s = 4	0.531	0.499	0.58	0.546
	s = 8	0.607	0.639	0.585	0.582

Received: 10 October 2026. Accepted: 09 November 2026. Published online: 11 November 2026.
Author:
Ştefan Ţălu, The Directorate of Research, Development and Innovation Management (DMCDI), The Technical University of Cluj-Napoca, Constantin Daicoviciu St., no. 15, Cluj-Napoca 400020, Cluj County, Romania, e-mail: stefan.talu@auto.utcluj.ro; stefan.talu1@gmail.com; ORCID: 0000-0003-1311-7657
This is an open-access article distributed under the terms of the Creative Commons Attribution License, which permits unrestricted use, distribution and reproduction in any medium, provided the original author and source are credited.
How to cite this article:
Ţălu, Ş. (2026). Quantitative multiscale analysis of spatial texture organization in liver histology of *Poecilia reticulata*. *Poeciliid Research, 16*(1), 75-105. https://doi.org/10.67784/0101